

# Probing the Early Stages of Low-Mass Star Formation in LDN 1689N: Dust and Water in IRAS 16293–2422A, B, and E

Ronald Stark

*Max-Planck-Institut für Radioastronomie, Auf dem Hügel 69, D-53121 Bonn, Germany*

*Sterrewacht Leiden, P.O. Box 9513, 2300 RA Leiden, The Netherlands*

Göran Sandell

*NASA Ames Research Center, MS 144-2, Moffett Field, CA 94035*

Sara C. Beck

*Department of Physics and Astronomy, Tel Aviv University, Ramat Aviv, Israel*

*Harvard-Smithsonian Center for Astrophysics, 60 Garden Street, Cambridge, MA 02138*

Michiel R. Hogerheijde

*Steward Observatory, The University of Arizona, 933 N. Cherry Ave, Tucson, AZ  
85721-0065<sup>1</sup>*

Ewine F. van Dishoeck

*Sterrewacht Leiden, P.O. Box 9513, 2300 RA Leiden, The Netherlands*

Peter van der Wal, Floris F. S. van der Tak, Frank Schäfer

*Max-Planck-Institut für Radioastronomie, Auf dem Hügel 69, D-53121 Bonn, Germany*

Gary J. Melnick, Matt L. N. Ashby

*Harvard-Smithsonian Center for Astrophysics, 60 Garden Street, Cambridge, MA 02138*

and

Gert de Lange

*Space Research Organisation of the Netherlands (SRON), P.O. Box 800, 9700 AV  
Groningen, The Netherlands*

## ABSTRACT

We present deep images of dust continuum emission at 450, 800, and 850  $\mu\text{m}$  of the dark cloud LDN 1689N which harbors the low-mass young stellar objects (YSOs) IRAS 16293–2422A and B (I16293A and I16293B) and the cold prestellar object I16293E. Toward the positions of I16293A and E we also obtained spectra of CO-isotopomers and deep submillimeter observations of chemically related molecules with high critical densities ( $\text{HCO}^+$ ,  $\text{H}^{13}\text{CO}^+$ ,  $\text{DCO}^+$ ,  $\text{H}_2\text{O}$ ,  $\text{HDO}$ ,  $\text{H}_2\text{D}^+$ ). To I16293A we report the detection of the  $\text{HDO}$   $1_{01}-0_{00}$  and  $\text{H}_2\text{O}$   $1_{10}-1_{01}$  ground-state transitions as broad self-reversed emission profiles with narrow absorption, and a tentative detection of  $\text{H}_2\text{D}^+$   $1_{10}-1_{11}$ . To I16293E we detect weak emission of subthermally excited  $\text{HDO}$   $1_{01}-0_{00}$ . Based on this set of submillimeter continuum and line data we model the envelopes around I16293A and E. The density and velocity structure of I16293A is fit by an inside-out collapse model, yielding a sound speed of  $a=0.7 \text{ km s}^{-1}$ , an age of  $t=(0.6-2.5)\times 10^4 \text{ yr}$ , and a mass of  $6.1 \text{ M}_\odot$ . The density in the envelope of I16293E is fit by a radial power law with index  $-1.0 \pm 0.2$ , a mass of  $4.4 \text{ M}_\odot$ , and a constant temperature of 16 K. These respective models are used to study the chemistry of the envelopes of these pre- and protostellar objects.

We made a large, fully sampled CO  $J=2-1$  map of LDN 1689N which clearly shows the two outflows from I16293A and B, and the interaction of one of the flows with I16293E. An outflow from I16293E as reported elsewhere is not confirmed. Instead, we find that the motions around I16293E identified from small maps are part of a larger scale fossil flow from I16293B. Modeling of the I16293A outflow shows that the broad HDO, water ground-state, and CO  $J=6-5$  and  $7-6$  emission lines originate in this flow, while the HDO and  $\text{H}_2\text{O}$  line cores originate in the envelope. The narrow absorption feature in the ground-state water line is due to cold gas in the outer envelope. The derived  $\text{H}_2\text{O}$  abundance is  $3\times 10^{-9}$  in the cold regions of the envelope of I16293A ( $T_{\text{kin}} < 14 \text{ K}$ ),  $2\times 10^{-7}$  in warmer regions of the envelope ( $> 14 \text{ K}$ ), and  $10^{-8}$  in the outflow. The HDO abundance is constant at a few  $\times 10^{-10}$  throughout the envelopes of I16293A and E. Because the derived  $\text{H}_2\text{O}$  and HDO abundances in the two objects can be understood through shock chemistry in the outflow and ion-molecule chemistry in the envelopes, we argue that both objects are related in chemical evolution. The  $[\text{HDO}]/[\text{H}_2\text{O}]$  abundance ratio in the warm inner envelope of I16293A of a few times  $10^{-4}$  is comparable to that measured in comets. This supports the idea that the  $[\text{HDO}]/[\text{H}_2\text{O}]$  ratio is determined in the cold prestellar core phase and conserved throughout the formation process of low-mass stars and planets.

*Subject headings:* stars: formation — ISM: clouds — ISM: jets and outflows —

## 1. Introduction

IRAS 16293–2422 is one of the best studied low-mass young stellar objects (YSOs) (Blake et al. 1994; van Dishoeck et al. 1995; Ceccarelli et al. 2000). It is deeply embedded in the LDN 1689N cloud in Ophiuchus (distance 160 pc) and classified as an extreme Class I/Class 0 YSO (Lada 1991). It is a low-luminosity ( $27 L_\odot$ , Walker et al. 1986) binary system (hereafter, I16293A and I16293B) with a separation of 840 AU (5'') and individual stellar masses of  $0.5 M_\odot$  (Mundy et al. 1992). Two powerful outflows emanate from the system. At least three physically and chemically different regions can be recognised in a 20'' (3000 AU) beam (van Dishoeck et al. 1995): (i) a cold, relatively low-density outer envelope ( $T_{\text{kin}} \simeq 10$ –20 K,  $n(\text{H}_2) \simeq 10^4$ – $10^5 \text{ cm}^{-3}$ ) which marks the transition into the extended parental cloud LDN 1689N; (ii) a warmer circumbinary envelope of size  $\sim 2000$  AU ( $T_{\text{kin}} \simeq 40$  K,  $n(\text{H}_2) \simeq 10^6$ – $10^7 \text{ cm}^{-3}$ ); and (iii) a warm, dense core of about 500–1500 AU ( $T_{\text{kin}} \geq 80$  K,  $n(\text{H}_2) \simeq 10^7 \text{ cm}^{-3}$ ) which traces the interaction of the outflow and the stellar radiation with the inner part of the circumbinary envelope. This picture emerged from excitation analysis of species tracing these distinct regions and conditions, assuming uniform temperatures and densities for each. Continuous descriptions of the density and temperature as function of radius in the collapsing envelope were developed by Ceccarelli et al. (2000) and Schöier et al. (2002) on scales from 30 to 5000 AU. In this Paper, we present new observations and modeling, that allows us to independently derive the density and temperature structure in the extended envelope around the (pre-) protostellar cores through continuum photometry and imaging of the dust, and heterodyne spectroscopy of the molecular gas. The resulting density and temperature distribution ranges from the warm inner envelope region (100 AU) to the coldest (12 K) outer envelope regions (7300 AU) and serves as a basis for excitation and abundance analysis of the line data.

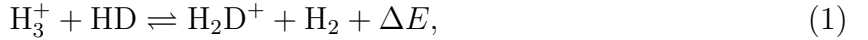
Another component of the IRAS 16293–2422 system is located 80'' east and 60'' south of I16293A. This small clump, I16293E, has strong  $\text{DCO}^+$ ,  $\text{NH}_3$ , and  $\text{NH}_2\text{D}$  emission (Wootten & Loren 1987; Mundy et al. 1990; Shah & Wootten 2001) connected to the I16293A core, and significant submillimeter continuum emission from dust (Sandell 1994). Single-dish observations of  $\text{NH}_3$  in a 40'' beam indicate a temperature  $T_{\text{kin}} = 12$  K (Mizuno et al. 1990). Millimeter-interferometric data, sampling smaller scales and less sensitive to the warmer

---

<sup>1</sup>Current Address: Sterrewacht Leiden, P.O. Box 9513, 2300 RA Leiden, The Netherlands

extended envelope, yield  $T_{\text{kin}} \simeq 8$  K and  $n(\text{H}_2) \simeq 1 \times 10^5 \text{ cm}^{-3}$  if homogeneous conditions are assumed (Shah & Wootten 2001). Because no far-infrared (FIR) or submillimeter point source has been found embedded in I16293E, it is classified as a pre-(proto)stellar core. In this Paper, we present submillimeter images that constrain the density structure of I16293E.

It is difficult to study chemical evolution in the early protostellar stages, because during collapse the temperature stays low at  $\sim 10$  K while the density increases to  $n(\text{H}_2) \geq 10^8 \text{ cm}^{-3}$ . Under these conditions the line emission of many molecules is dominated by a warmer outer envelope around the prestellar core. Also, many molecules in the cold core will condense on dust grains. Eventually, only  $\text{H}_2$ ,  $\text{H}_3^+$ , and their isotopomers  $\text{HD}$  and  $\text{H}_2\text{D}^+$  will remain in the gas phase. This leads to a significant enhancement of  $\text{H}_2\text{D}^+$  through the deuterium exchange reaction



since the backward reaction becomes negligible at low temperatures (Smith et al. 1982; Herbst 1982).  $\text{H}_2\text{D}^+$  is thought to play a pivotal role in the deuteration of molecules (Watson et al. 1976; Millar et al. 1989) and the detection of  $\text{H}_2\text{D}^+$  in the Class 0 YSO NGC 1333 IRAS 4A (Stark et al. 1999) is an important confirmation of the cold gas-phase chemical networks. The  $\text{H}_2\text{D}^+$  enhancement is reflected in the high abundance ratios that are generally observed of, e.g.,  $[\text{DCO}^+]/[\text{HCO}^+]$ ,  $[\text{NH}_2\text{D}]/[\text{NH}_3]$ ,  $[\text{DCN}]/[\text{HCN}]$ , and  $[\text{N}_2\text{D}^+]/[\text{N}_2\text{H}^+]$  in cold prestellar cores and Class 0 YSOs (e.g., Guélin et al. 1982; Olberg et al. 1985; Wootten 1987; Butner et al. 1995; Williams et al. 1998; Bergin et al. 2002). Models predict that in the collapse stage the abundances of many deuterated radicals and molecules increase sharply after their non-deuterated versions start to get heavily depleted on dust grains, then reach a peak and start to decrease as the deuterated molecules too condense on the dust (e.g., Brown & Millar 1989; Rodgers & Millar 1996). Reactions with atomic deuterium on the grain surface may further enhance the abundance of deuterated species in the ice (Tielens 1989; Brown & Millar 1989). After the formation of a YSO, the condensed molecules may evaporate from grains, resulting in a temporary increase in the gas-phase deuteration fraction. The deuteration may decline after  $\sim 10^4$  years (Rodgers & Millar 1996) when higher temperature chemistry becomes effective. In addition, in such hot ( $T_{\text{kin}} \simeq 100\text{--}200$  K) regions the reversal of reaction (1) becomes dominant and very little new fractionation is expected to occur. We report in this Paper observations of several key deuterated species in I16293A and I16293E.

Water is an important species in the early stages of star formation.  $\text{H}_2\text{O}$  is the most important hydride molecule in oxygen chemistry and models predict that  $\text{H}_2\text{O}$  plays a dominant role in the energy balance and chemical evolution during star formation. Water will have the largest abundance and excitation contrast between the protostellar source and the surrounding cloud (e.g., Ceccarelli et al. 1996; Doty and Neufeld 1997). Measurements of the rotational and ro-vibrational transitions of  $\text{H}_2\text{O}$  in star-forming regions have recently become

available from the Infared Space Observatory (ISO; e.g., Helmich et al. 1996a; Ceccarelli et al. 2000) and the Submillimeter Wave Astronomical Satellite (SWAS; e.g., Ashby et al. 2000; Snell et al. 2000; Neufeld et al. 2000). In particular the heterodyne velocity-resolved measurements of the ground-state transition of ortho-H<sub>2</sub>O with SWAS allow a direct determination of the water abundance throughout the envelope. The HDO 1<sub>01</sub>–0<sub>00</sub> ground-state transition at 465 GHz ( $E_u = 23.2$  K,  $n_{\text{crit}} \geq 10^8$  cm<sup>-3</sup> for  $T_{\text{kin}} \leq 50$  K, Green 1989) is an excellent tracer of high density gas at low temperatures where the abundance of HDO relative to water is enhanced. Ground-based observations of the HDO ground-state transition are still very sparse. To date, this transition has only been observed in the high-mass star-forming regions Orion-KL (Schulz et al. 1991), W3(OH), and W3(H<sub>2</sub>O) (Helmich et al. 1996b). The latter study indicates that the [HDO]/[H<sub>2</sub>O] abundance ratio is comparable to that found in hot cores and is not a sensitive indicator of the evolutionary stage in high-mass star formation. This could mean either that the W3 cloud always stayed warm or that the [HDO]/[H<sub>2</sub>O] ratio retrusn to thermal equilibrium faster than ratios like [DCN]/[HCN] (Helmich et al. 1996b). For a low-mass Class 0 YSO like I16293A the situation may be different, because the time scale to reach steady-state may be much longer. In this Paper, we present observations of HDO and H<sub>2</sub>O of I16293A and E.

In this paper we present a detailed study of the physical and chemical structure of the low-mass star-forming cloud LDN 1689N with particular emphasis on the H<sub>2</sub>O/HDO chemistry and deuterium fractionation. We present extensive submillimeter continuum photometry and maps revealing the warm and cold dust around I16293A, B and I16293E (§2.1). We report the detection of the ground-state lines of (deuterated) water and a tentative detection of H<sub>2</sub>D<sup>+</sup> toward I16293A as well as weak HDO emission in the prestellar core I16293E (§2.2). These data are combined with pointed observations of CO and HCO<sup>+</sup> isotopomers to determine the temperature and density structure throughout the envelope (§3). We address the two outflows and their origin in §4. Our deep observations of the HDO and H<sub>2</sub>O ground-state transitions are used to study the [HDO]/[H<sub>2</sub>O] ratio throughout the envelope (§5.1). A simple chemistry network is used to model the deuterium chemistry and in particular the water fractionation (§5.2). Finally, we discuss the evolutionary difference between I16293A, I16293B, and I16293E (§6), and summarize the conclusions in §7.

## 2. Observations and Data Reduction

### 2.1. Submillimeter Continuum

All continuum observations were made with the James Clerk Maxwell Telescope (JCMT), using the single channel bolometer UKT14 and the versatile Submillimetre Common-User

Bolometer Array (SCUBA) under good weather conditions. The UKT14 measurements were done during the winters of 1991–1993. This instrument was for a long time the common-user bolometer system and is described in Duncan et al. (1990). It was replaced in 1997 by SCUBA which was designed both for photometry and fast mapping (Holland et al. 1998).

The photometry of I16293E was done with UKT14 during Spring 1993. The chop throw was  $90''$  in Declination and the calibrators were Uranus and the nearby secondary calibration standard I16293A (Sandell 1994). The results are given in Table 1. UKT14 maps were obtained at 1.1 mm,  $800\,\mu\text{m}$ ,  $750\,\mu\text{m}$ ,  $450\,\mu\text{m}$ , and  $350\,\mu\text{m}$  during several observing runs in 1991 and 1992. Most of these maps have poor sensitivity and were mainly used to derive the submillimeter position of I16293A. However, even with the somewhat limited signal-to-noise (S/N) these provide a better estimate of the background subtracted flux of I16293A than single position photometry.

At  $800\,\mu\text{m}$  we attempted to go deep and completely map the dust cloud surrounding the bright submillimeter source. Because the dust emission is very extended (see the  $850\,\mu\text{m}$  SCUBA map in Fig. 1) we combined six maps of the region, centered on I16293A or I16293E. Each map was bound by pointing observations of the nearby blazars 1514–241 and 1730–130. Typical pointing drifts were less than  $2''$ . These errors were removed in the data reduction process assuming that the pointing drifts linearly in Azimuth and Elevation as a function of time. All maps were made on-the-fly, scanned in Azimuth with a cell size of  $4''$  and a chop throw of  $40''$  in the scan direction. With a single pixel instrument it is difficult to map such an extended region. The final map was therefore reduced with the Dual Beam Maximum Entropy (DBMEM) algorithm written by John Richer (Richer 1992) for JCMT. The DBMEM map was baseline subtracted and recalibrated by using the integrated intensity in a  $60'' \times 60''$  area around I16293A from maps reduced with NOD2 (Haslam 1974; Emerson et al. 1979). The  $800\,\mu\text{m}$ -map is shown in Fig. 1 (top panel). From comparison with SCUBA maps (see below), it is clear that the  $800\,\mu\text{m}$ -map has failed to recover the faint, relatively uniform, low-level emission surrounding both cloud cores. This does not affect the morphology of the map, but does have a large effect on integrated intensities of the surrounding LDN 1689N cloud. The low-level emission is missing because the  $800\,\mu\text{m}$ -maps were taken with the same rather short chop throw, and the individual maps have a noise level comparable or higher to that of the low-level extended emission. It is also well known that the NOD2-algorithm is not very sensitive to relatively uniform extended emission on spatial scales of several times the chop throw (Emerson et al. 1979).

Additional maps were obtained with SCUBA during Spring 1997 as part of commissioning jiggle- and scan-map observing modes. We have complemented these maps with additional maps obtained from the JCMT archive in the time period 1997–1998. All maps

were taken under excellent sky conditions (atmospheric opacities  $\tau_{225\text{ GHz}} < 0.04$ ), and all the maps in the archive were taken with a  $120''$  chop throw, typically in Azimuth. Most of the maps of I16293E were also obtained with a  $120''$  chop.

The pointing was checked before and after each map using the same blazars as for our UKT14 observations. Some of the archive maps, however, were taken without pointing observations. These were aligned with the pointing corrected average before adding them into the final data set. Calibration and beam characterization is based on beam maps of Uranus obtained with the same chop throw. The Uranus maps give a Half Power Beam Width of  $14.5''$  and  $7.8''$  for  $850\text{ }\mu\text{m}$  and  $450\text{ }\mu\text{m}$ , respectively.

Both the I16293A, B and I16293E cloud cores are rather extended and no map is completely free of emission in the off positions. Any bolometer that showed evidence for or was suspected of being contaminated by the chop was therefore blanked in the data reduction. Although this was done as carefully as possible, it is clear that the outskirts of our final mosaiced image (Fig. 1) may still be affected, especially since the dust emission extends beyond the area we mapped to the north and northeast of both I16293A and I16293E. The cloud core surrounding I16293E also extends further east than is covered by our maps.

The basic data reduction was done using the SCUBA software reduction package SURF (Jenness 1998) as explained in the SCUBA Map Reduction Cookbook (Sandell 2001). In total we used 16 data sets for the  $850\text{ }\mu\text{m}$  map and 13 for the  $450\text{ }\mu\text{m}$  map. In the final coadd we adjust the pointing in each map (shift and add) to ensure that the final map is not broadened by small pointing errors. The rms noise levels in the final maps are difficult to estimate, because there are no emission-free regions in the maps, but we estimate them to be below  $20\text{ mJy beam}^{-1}$  at  $850\text{ }\mu\text{m}$  and below  $80\text{ mJy beam}^{-1}$  at  $450\text{ }\mu\text{m}$ .

The final maps were converted to FITS and exported to MIRIAD (Sault 1995) for further analysis. In order to correct for the error beam contribution, especially at  $450\text{ }\mu\text{m}$ , we deconvolved the maps using clean and spherically symmetric model beams derived from beam maps of Uranus observed in stable night time conditions. At  $850\text{ }\mu\text{m}$  we use HPBWs of  $14.5''$ ,  $55''$ , and  $150''$ , with amplitudes of 0.985, 0.014 and 0.001, respectively. At  $450\text{ }\mu\text{m}$  the HPBWs are  $7.8''$ ,  $34''$ , and  $140''$ , with amplitudes of 0.964, 0.029, and 0.007, respectively. The final maps were restored with a  $14''$  beam at  $850$  and an  $8''$  beam at  $450\text{ }\mu\text{m}$ . The peak flux densities in the restored maps are  $16.0\text{ Jy beam}^{-1}$  and  $76.1\text{ Jy beam}^{-1}$  toward I16293A at  $850$  and  $450\text{ }\mu\text{m}$ , respectively, while the peak fluxes of I16293E are  $1.4\text{ Jy beam}^{-1}$  and  $4.35\text{ Jy beam}^{-1}$  at  $850$  and  $450\text{ }\mu\text{m}$ , respectively.

## 2.2. Molecular line observations

Spectra of CO  $J=2-1$  (230.538000 GHz) and isotopomers, as well as the  $J=3-2$  transitions of DCO $^+$  (216.112605 GHz), HCO $^+$  (267.557619 GHz), and H $^{13}$ CO $^+$  (260.255478 GHz) toward I16293A and I16293E were retrieved and reduced from a search of all released data in the JCMT archive at the Canadian Astronomy Data Center taken with the SIS receiver RxA2 and its successor RxA3. Deep observations of the HDO  $3_{12}-2_{12}$  (225.896720 GHz) and  $2_{11}-2_{12}$  (241.561550 GHz) lines were made with the receiver RxA3 in 2001 April. We also acquired a large, fully sampled map in the CO 2–1 line which is centered on I16293E and covers the outflows from I16293A and B. The map was made on-the-fly with a bandwidth of 125 MHz, a sampling of 5" in the scan direction, and a cross-scan step size of 10". The final map was made from a series of sub-maps scanned either in RA or Dec. The integration time per point was 5 seconds, but in poor weather conditions we often made multiple coverages. All observations were done in position switch mode with the reference position 600" or 800" west of the submillimeter position of I16293E. At the same time we have also obtained spectra toward I16293A, which is a pointing and spectral line standard. The relative calibration of the spectra of the CO 2–1 map is accurate within 5%, because we overlapped the sub-maps. In 1999 April we obtained additional deep spectra of CO and  $^{13}$ CO 2–1 (220.398677 GHz) at the peak positions in the outflow lobes in order to get more accurate estimates of the  $^{12}$ CO optical depth in the high velocity gas. Most of the spectra were obtained with a bandwidth of 125 MHz, corresponding to a velocity resolution of 0.1 km s $^{-1}$ . The spectra are calibrated in  $T_{\text{MB}}$  (I16293A) or  $T_R^*$  (I16293E) and shown in Figs. 2 and 3. The results of gaussian fits to the line profiles are summarised in Table 2. For some of the lines with symmetric profiles (e.g., HDO) the emission and the absorption components were fitted separately. For most of the complex line profiles we only list the integrated emission and the velocity of the maximum self-absorption. Note that the phase-lock instability of RxA2 and RxA3 may cause an instrumental broadening up to 0.5 km s $^{-1}$ .

The N<sub>2</sub>H $^+$   $J=4-3$  (372.672509 GHz), H<sub>2</sub>D $^+$   $1_{10}-1_{11}$  (372.421340 GHz), DCO $^+$  5–4 (360.169881 GHz), HCO $^+$  4–3 (356.734288 GHz), and H $^{13}$ CO $^+$  4–3 (346.998540 GHz) rotational transitions were observed in 2000 April with the JCMT using the dual channel SIS receiver RxB3. The receiver was operated in single side band (SSB) mode where the image side band is rejected and terminates in a cold load. The main beam efficiency at these frequencies is about 60%, while the beam width is 14–13" for 345–372 GHz. The lines were observed in beamswitching mode switching over 180". The N<sub>2</sub>H $^+$  and H<sub>2</sub>D $^+$  lines were observed simultaneously with relatively good atmospheric transparency ( $\tau_{225 \text{ GHz}} \simeq 0.05$ ), but with only 30 minutes of useful integration time above an elevation of 40 degrees. RxB3 was changed to tunerless mixers in 1999 and the performance near the upper band edge has decreased dramatically with respect to Stark et al. (1999). Nevertheless we have tentatively

detected the  $\text{H}_2\text{D}^+$  ground-state line (Fig. 2).

The HDO  $J=1_{01}-0_{00}$  ground-state transition (464.924520 GHz) was observed in 1998 July at the JCMT during a night of excellent submillimeter transparency with a zenith optical depth at 225 GHz below 0.05. The dual channel, dual band 460/660 GHz SIS receiver RxW was used in SSB mode with the Digital Autocorrelator Spectrometer (DAS) backend. The DAS was split in two parts of 125 MHz with a spectral resolution of 189 kHz ( $=0.12 \text{ km s}^{-1}$  at 465 GHz). The HDO line was observed in the upper side band, and SSB system temperatures including atmospheric losses were  $T_{\text{sys}} \lesssim 1000 \text{ K}$ . The beam size is about  $11''$  at 465 GHz and the main beam efficiency was measured to be about 50%. We observed the HDO line toward I16293A in position switch mode with the same reference as above. We also observed the line in beam switch mode, switching over  $\pm 180''$  in Azimuth. These spectra show the same profile as the position switched ones, but only the beam switched spectra clearly reveal the level of the continuum emission from the dust heated by the YSO. All spectra were coadded and corrected for the continuum level. In addition, deep spectra of the HDO line toward I16293E were obtained in position switch mode. The data were calibrated similarly to the RxA2 and A3 observations.

The  $\text{H}_2\text{O}$   $1_{10}-1_{01}$  ground-state transition (556.936002 GHz) was observed in 1999 August with SWAS (Melnick et al. 2000). The receiver consisted of a Schottky diode mixer resulting in a double sideband system temperature of about 2200 K. The back-end was an Acousto Optical Spectrometer with a 1.4 GHz bandwidth and a velocity resolution of  $\leq 1 \text{ km s}^{-1}$ . The beam width is about  $4'$ . The  $\text{H}_2\text{O}$  line was observed in position switch mode, switching to an emission free reference position  $1.5^\circ$  away. The total (on+off) integration time was 23.5 hrs, yielding a noise level of  $T_{\text{A}}^*(\text{rms}) = 0.01 \text{ K}$ .

The CO  $J=6-5$  (691.473076 GHz) and  $7-6$  (806.651806 GHz) transitions toward I16293A have been taken with the JCMT using the RxW receiver in 1999 August and with the MPIfR/SRON 800 GHz SIS receiver in 2000 April, respectively, under good atmospheric conditions. The beam parameters at these frequencies were determined from observations of Mars. The main beam efficiencies are about 0.3 and 0.24, and the beam sizes (FWHM) are  $8''$  and  $6''$  at 691 GHz and 806 GHz, respectively.

### 3. Results and Analysis

#### 3.1. Submillimeter Continuum: Morphology

IRAS 16293–2422 was found to be a binary system in 6 cm and 2 cm VLA observations by Wootten (1989). The two components are separated by  $5''$  (840 AU) with a position

angle of  $PA = 135^\circ$ . High resolution millimeter observations (Mundy et al. 1992; Looney et al. 2000) also resolve the IRAS source into a binary system, in good agreement with the VLA data. The southern component (A or MM1) is more extended in millimeter continuum and is associated with dense gas, high velocity emission and  $H_2O$  masers (Mundy et al. 1992; Choi et al. 1999; Looney et al. 2000) suggesting that it is the more active component of the binary system. The northern component, B or MM2, is very compact both at centimeter and millimeter wavelengths, and has a surprisingly steep spectrum,  $\alpha = 2.3 \pm 0.3$  (Mundy et al. 1992). It is brighter than A at both 1.3 cm and 2.7 mm (Estelella et al. 1991; Mundy et al. 1992; Schöier et al. 2003).

We resolve IRAS 16293–2422 in all maps with a FWHM  $\sim 9.6'' \times 5.7''$  at  $450\,\mu\text{m}$  with  $PA = 152^\circ$ , and find it slightly more extended at  $800$  and  $850\,\mu\text{m}$  with  $PA = 145^\circ$  and  $147^\circ$ , respectively. The corresponding size at  $850\,\mu\text{m}$  is  $\sim 10.0'' \times 7.4''$ . The emission is centered on A to within  $1''$  in all single dish maps. The same is true for the lower S/N single-coverage UKT14 maps at  $1.1\,\text{mm}$ ,  $750$ ,  $450$  and  $350\,\mu\text{m}$ . In Fig. 4, we show the azimuthally averaged flux densities of I16293A and its surrounding envelope, and of the prestellar core I16293E. The intensity falls off much more rapidly for I16293A than for the prestellar core I16293E at radii  $r < 20\text{--}30''$ , beyond where the slope flattens out to be similar to the prestellar core.

The size and  $PA$  seen in our submillimeter maps agree within the errors with the  $C^{18}\text{O}$  emission mapped by Mundy et al. (1992) with OVRO and differs in  $PA$  from the alignment of the two submillimeter sources A and B. In fact, neither the  $C^{18}\text{O}$  emission nor the  $450\,\mu\text{m}$  emission shows any clear enhancement at the B position which is the stronger continuum source in the wavelength range  $1.3\,\text{cm}$  to  $2.7\,\text{mm}$ . At longer wavelengths ( $850$  and  $800\,\mu\text{m}$ ) the  $PA$  approaches that of the binary suggesting that at these wavelengths the emission from B is still significant. However, none of our maps lines up exactly with the binary, which is what one would expect if the emission originated from a circumbinary disk. Looney et al. (2000) claim that their high resolution maps show that the dust emission is aligned with the binary. However, considering the S/N in their map, one could equally well interpret their result as a circumstellar disk surrounding A with a position angle similar to that seen in  $C^{18}\text{O}$  and  $450\,\mu\text{m}$ , and B as a separate but partly overlapping source. Their observations show that about 90% of the dust emission surrounding A is spatially extended, while B is largely unresolved at all spatial scales they could measure. Schöier et al. (2003) observed the continuum at  $1.37\,\text{mm}$  with OVRO at  $3''$  resolution and find that I16293A and I16293B both have a disk with diameter  $< 250\,\text{AU}$ .

We conclude that the submillimeter dust continuum and most of the molecular emission are centered on A and have a disk-like morphology. The dust disk is surrounded by faint extended emission from the surrounding dark cloud core which falls off rather rapidly toward

the south and southwest. The dark cloud core is more extended toward the north and northeast ( $\sim 70''$ ), and in the west a narrow dust bridge connects it to I16293E (see Fig. 1).

In contrast, I16293E is very extended and has a much flatter emission profile than I16293A (see Figs. 1, 4). The peak emission is centered on  $\alpha_{2000.0} = 16^h 32^m 28.84^s$ ,  $\delta_{2000.0} = -24^\circ 28' 57.0''$  with a roughly triangular emission region around the peak. It has a ridge-like structure at 450  $\mu\text{m}$  (see Fig. 5). The integrated fluxes (corrected for error lobe contribution) are 20 Jy and 133 Jy at 850 and 450  $\mu\text{m}$ , respectively, in a 50'' radius (8000 AU). In order to perform single position photometry we also made gaussian fits to our submillimeter images resulting in a source size of  $32'' \times 17''$  with  $PA = 3 \pm 5^\circ$  superposed on a more extended background. This source size was used to convert our photometry into integrated intensities for further analysis.

### 3.2. Excitation Analysis

#### 3.2.1. The Protostellar Disk Around I16293A

The submillimeter maps allow us to derive a mass estimate for the dust which is more accurate than previous values. I16293A has been used extensively as a secondary calibrator for submillimeter continuum observations at JCMT (Sandell 1994), and has accurately known fluxes in all submillimeter bands. Although some of our UKT14 maps have relatively poor S/N, they still allow us to make a reliable estimate of the flux density of the compact dust disk, because the underlying emission from the envelope can be determined and subtracted. This is not possible from photometry data (Sandell 1994). In Table 1 we list the integrated fluxes for I16293A from two-dimensional Gaussian fits to our maps after subtraction of the extended envelope emission. We have not mapped the region at 1.3 mm, but instead use data from Mezger et al. (1992) who derived the integrated flux in a similar fashion.

We could use the SCUBA data together with co-added IRAS data at 100 and 60  $\mu\text{m}$  to constrain the dust temperature, but it is clear from our submillimeter maps that the arcmin size of the IRAS beam will also include emission from the surrounding dark cloud, so to include the IRAS data we should do a two component fit and simultaneously solve for the dust envelope and the disk. Instead, we take a simpler approach. We solve for each separately and use the IRAS data to make sure that the results we get are plausible. Our deep 850 and 450  $\mu\text{m}$  SCUBA maps predict that about half or more of the continuum emission seen by IRAS is likely to come from the envelope surrounding the dust disk. We therefore divide the IRAS 100  $\mu\text{m}$  emission into halves and assume one half to originate in a compact  $\leq 7.4''$  disk and the rest from a cooler cloud envelope around the protostar.

If we assume that the dust grains can be characterized by a single temperature,  $T_d$ , the flux density  $S_\nu$  at frequency  $\nu$  can be written as

$$S_\nu = \Omega_s B_\nu(T_d)(1 - e^{-\tau_\nu})e^{-\tau_{\text{env}}}, \quad (2)$$

where  $\Omega_s$  is the source solid angle,  $B_\nu(T_d)$  is the Planck function,  $\tau_\nu$  the optical depth of the disk, and  $\tau_{\text{env}}$  optical depth of the envelope. We assume that the envelope is optically thin at submillimeter wavelengths ( $\tau_{\text{env}} \ll 1$ ). We write  $\tau_\nu$  as

$$\tau_\nu = \tau_0 \left( \frac{\nu}{\nu_0} \right)^\beta, \quad (3)$$

where  $\tau_0$  is the dust optical depth at frequency  $\nu_0$ , and  $\beta$  is the dust emissivity describing how the dust opacity ( $\kappa_\nu \propto \tau_\nu$ ) changes with frequency (Hildebrand 1983). We adopt the Hildebrand (1983) opacity ( $\kappa_{1.2 \text{ THz}} = 0.1 \text{ cm}^2 \text{ g}^{-1}$ ) and assume a gas-to-dust ratio of 100. It is now straight forward to do a least-squares fit to equation (2). Since we mapped the whole cloud, we know  $\Omega_s$ , and use this to constrain the fit. We omit flux densities measured at 3 mm with aperture synthesis telescopes, because these resolve out the extended emission and may also include free-free emission.

For the submillimeter disk of I16293A we derive a dust temperature  $T_d = 40 \pm 1 \text{ K}$  (see Fig. 6),  $\beta=1.6$  and a source size of about  $5''$ . In order to make sure that these values are not determined by our assumed partitioning of the IRAS 100  $\mu\text{m}$  flux estimate, we also repeated the fit omitting the 100  $\mu\text{m}$  data and got similar results. Our fit to the dust disk is not affected by the 100  $\mu\text{m}$  data because the dust emission in this source starts to become optically thin in the (sub) millimeter regime,  $\tau_{850 \mu\text{m}} \sim 0.42$ , which acts as a constraint for the dust temperature. This is unusual as dust emission is usually optically thin at (sub) millimeter wavelengths and does not provide any constraints on the dust temperature, unless  $\beta$  is known. From the fit we derive a total mass of  $1.8 \text{ M}_\odot$  corresponding to an average density of  $n(\text{H}_2) \geq 10^9 \text{ cm}^{-3}$ , and a bolometric luminosity of  $16.5 \text{ L}_\odot$ . The uncertainty in the mass, due to uncertainties in the fitted  $T_d$  and  $\beta$ , is of the order of  $0.3 \text{ M}_\odot$ . The continuum measurements of Schöier et al. (2003) show that the source size is smaller than  $3''$ . Schöier et al. assume optically thin emission at 1.37 mm, and a dust temperature of 40 K and derive a lower limit to the mass of  $0.25 \text{ M}_\odot$ . Our derived mass of the dust disk is in the mid-range of the values quoted by Mundy et al. (1986). Our fit appears to slightly overestimate the flux densities at long wavelengths, which indicates that the data cannot completely be described by a single dust temperature.

### 3.2.2. The Prestellar Core I16293E

Since the continuum emission traces the integrated density along the line of sight, the SCUBA images can be used to derive the density distribution. We used the azimuthally averaged radial flux density of the continuum maps at 450 and 850  $\mu\text{m}$  to determine the radial density structure of I16293E. Figure 4 shows the radial emission profiles of this prestellar core; it is clearly seen that both emission profiles are well described by a power-law. Instead of the dust density we will use the  $\text{H}_2$  volume density as parameter in determining the density distribution. We adopt a dust-to-gas ratio of 1 : 100 and a power-law  $\text{H}_2$  density distribution of the form  $n(r) = n_0(r/1000 \text{ AU})^{-p}$ , where  $n_0$  is the  $\text{H}_2$  density at the arbitrary chosen radius of 1000 AU. Similarly, we adopt a dust temperature  $T_d$  distribution following a radial power-law with index  $q$  and temperature  $T_0$  at  $r = 1000 \text{ AU}$ . The dust emissivity is assumed to be of the form equation (3).

The free parameter set of this model ( $n_0$ ,  $p$ ,  $T_0$ ,  $q$ ,  $\beta$ ) is constrained by the total submillimeter flux, the radial emission profiles, and the spectral index between 450 and 850  $\mu\text{m}$ , respectively. A  $\chi^2$  minimalization between the core model emission and the data yields best-fit parameters  $p = 1.0 \pm 0.2$  for both the 450  $\mu\text{m}$  and 850  $\mu\text{m}$  images,  $n_0 = 1.6 \times 10^6 \text{ cm}^{-3}$ , and  $\beta = 2.0$ . The outer radius of the core was set to 8000 AU, the only value of  $R_{\text{out}}$  which allows a density profile fit with a single power-law index  $p$ . The above density structure yields a core mass  $M_{\text{core}}(\text{H}_2) = 4.35 \text{ M}_\odot$ . From these results we infer an isothermal dust temperature  $T_d = 16 \text{ K}$ , i.e.  $q = 0$ . We apply this temperature to the region  $r < 1000 \text{ AU}$  while for  $1000 \text{ AU} < r < 8000 \text{ AU}$  we let the temperature gradually rise to 20 K to include the transition of the dark core to the diffuse ISM where the temperature is determined by the interstellar radiation field. This temperature structure gives a good fit to the observed radial emission profiles. Note that the continuum emission is a convolution of the density and temperature, so the derived density and temperature structures are degenerate, e.g., a constant temperature  $T_d = 25 \text{ K}$  and  $n_0 = 1.1 \times 10^6 \text{ cm}^{-3}$  also fits the emission profiles. However, the low-end  $T_d$  and high-end  $n$  fit yields a plausible physical description to this prestellar core and best fit to the observed HDO emission (see below).

The IRAS 100  $\mu\text{m}$  data were not used to further constrain the above parameter-set, IRAS was not sensitive to continuum emission from dust with  $T_d < 18 \text{ K}$ . On the other hand the SCUBA emission reflects a convolution of density and temperature along the line-of-sight. Thus, a cold high density region with  $T_d \ll 18 \text{ K}$  can easily be hidden in the center of the core since a less dense warmer envelope component will always dominate the observed continuum emission. In general such a region will be hard to detect in continuum emission as well as in line emission. In the latter case one would need a transition of a species with a high critical density and low excitation temperature which is uniquely tracing the coldest

and densest part at the heart of the core and is not depleted. Deuterated molecules, and in particular the ground-state transitions of HDO, are excellently suited to trace such regions (see §1 and below).

The inferred radial density and temperature structures from the dust are used to calculate the abundance profiles for the observed single dish observations of C<sup>17</sup>O, C<sup>18</sup>O, DCO<sup>+</sup>, HCO<sup>+</sup>, H<sup>13</sup>CO<sup>+</sup>, and HDO. The modeling of the molecular excitation and line radiative transfer uses a spherically symmetric Monte Carlo method (Hogerheijde & van der Tak 2000). The core was divided in 40 concentric shells. All shells were found to be optically thin at the modeled transitions of the molecules. We assume  $T_{\text{kin}} = T_{\text{d}}$  throughout the core and adopt for each line a constant local turbulent linewidth. After convergence of the level populations was reached, the spectral line profile of the observed transition of each molecule was calculated for the appropriate beam. The calculations were done iteratively starting with an educated guess for the abundance and the turbulent linewidth, until a best fit of the modeled line profiles to the observed spectra was established.

Our model spectra fit the observed emission profiles for all relevant molecules (Fig. 7) and yield the following abundances for the CO-isotopomers:  $[\text{C}^{18}\text{O}]/[\text{H}_2] = 3 \times 10^{-8}$  and  $[\text{C}^{17}\text{O}]/[\text{H}_2] = 9 \times 10^{-9}$ . Adopting standard CO isotopomer ratios  $[\text{CO}]/[\text{C}^{18}\text{O}] = 500 : 1$ , and  $[\text{CO}]/[\text{C}^{17}\text{O}] = 2500 : 1$  (Wilson 1994), our derived abundances imply that CO is depleted by a factor of about ten with respect to the standard abundance.

The width and strength of the observed HDO ground-state emission line is well fit by a  $[\text{HDO}]/[\text{H}_2]$  abundance ratio of  $2 \times 10^{-10}$ . Note that the derived turbulent linewidth of the HDO line is much lower than that of the other lines. It is expected that the turbulent line width is roughly the same for all molecular species when observed with similar angular resolution if they are distributed similarly throughout the core. This is in fact the case for the other molecules observed with beams of about 15'' (DCO<sup>+</sup>, HCO<sup>+</sup>, etc.) for which we obtain an average value of  $0.7 \pm 0.1 \text{ km s}^{-1}$ . Although the weak HDO emission has a S/N of only 3, its narrowness suggests that it resides in the innermost region of the I16293E core. In this cold region ( $T_{\text{K}} \leq 16 \text{ K}$ ) the abundance of a deuterated species like HDO is expected to be enhanced through equation (1), while non-deuterated molecules are expected to be depleted (§1). A higher S/N HDO spectrum is required to confirm this.

The best fit to the HCO<sup>+</sup> 3–2 line yields an abundance  $[\text{HCO}^{+}]/[\text{H}_2]$  of  $1 \times 10^{-10}$ . The H<sup>13</sup>CO<sup>+</sup> 3–2 emission can be reproduced for a constant abundance of  $2 \times 10^{-11}$  throughout the core, and the DCO<sup>+</sup> 3–2 line fit yields an abundance of  $5 \times 10^{-11}$ . Note that  $[\text{DCO}^{+}]/[\text{H}^{13}\text{CO}^{+}] = 2.5$ , that is the DCO<sup>+</sup> abundance is larger than that of H<sup>13</sup>CO<sup>+</sup>. Assuming  $[\text{CO}]:[\text{CO}^{+}] = 65:1$  (Wilson 1994), we find that HCO<sup>+</sup> is depleted by a factor of about 10. Table 3 summarizes the inferred abundances and local turbulent linewidths.

### 3.2.3. The Envelope Around I16293A

In this section we determine a radial density and temperature structure for the YSO envelope using an inside-out collapse power-law density structure where the slope of the density and the velocity depend on the location of the collapse expansion wave.

We assume that the dust temperature follows a radial power law. Such a distribution is expected for a spherical cloud with an embedded heating source in its center. Together with the FIR luminosity and distance of 160 pc, the temperature distribution is constrained from the total observed submillimeter continuum emission from the disk and the envelope (Table 1). The inferred temperature profile ranges from  $T_d = 115$  K at the inner radius  $r_{\text{in}} = 100$  AU, to  $T_d = 12$  K at the outer radius  $r_{\text{out}} = 7300$  AU.

We use the spherically symmetric self-similar solution of a collapsing cloud core derived by Shu (1977) to determine the density profile. This model is characterised by only two parameters: the sound speed  $a$ , and the time  $t$  since the collapse starts at the center at  $t = 0$ . The initial stationary density distribution is an isothermal sphere where the density is proportional to  $r^{-2}$ . At a time  $t$  after the onset of collapse, the head of the collapse expansion wave is radius  $r_{\text{CEW}} = at$ . Inside this radius the velocity field varies from stationary to free fall,  $V \propto r^{-\frac{1}{2}}$ , while the density varies as  $n \propto r^{-\frac{3}{2}}$ . We determine the infall parameters independently from the molecular spectroscopic data as well as from the dust continuum measurements. We start with the former.

We do not use RxA2 observations, which instrumentally broadens the lines, but only 345 GHz window spectra to determine the infall parameters. Earlier studies often used emission lines from lower rotational transitions of  $\text{HCO}^+$  or  $\text{H}^{13}\text{CO}^+$ . Our line profiles of  $\text{HCO}^+ 4-3$  and  $\text{H}^{13}\text{CO}^+ 4-3$  are complex with excess emission at the red and blue wings of the doubly peaked emission profile, respectively (see below). This points to a contribution by the outflow(s). The red and blue wings of the  $\text{DCO}^+ 5-4$  spectrum are symmetric, and we therefore use this line profile to constrain the parameter set  $a$  and  $t$ . These parameters respectively determine the width and integrated line intensity of the profile.

A good fit to the wings of the  $\text{DCO}^+ 5-4$  emission is found for  $t = 2.5 \times 10^4$  yr,  $a = 0.7$  km s $^{-1}$ , and a constant radial abundance  $[\text{DCO}^+]/[\text{H}_2] = 2 \times 10^{-11}$  (Fig. 8). This yields an envelope  $\text{H}_2$  mass  $M = 6.1 M_\odot$  within a radius of 7300 AU. Note that the absorption can easily be fitted by adding a cold outer shell where the temperature has dropped to  $T_d < 10$  K. Our derived stationary envelope mass corresponds well with the mass derived by Schöier et al. (2002) of  $M = 5.4 M_\odot$  inside  $r_{\text{out}} = 8000$  AU, but is as much as a factor of four higher than the masses derived by Ceccarelli et al. (1996) ( $M = 1.88 M_\odot$ ,  $r_{\text{out}} = 5307$  AU) and Narayanan et al. (1998) ( $M = 2.3 M_\odot$ ,  $r_{\text{out}} = 6000$  AU). In Fig. 9 we plot the

calculated dust and density profiles. For comparison we also plot the independently derived density and temperature profiles from Schöier et al. (2002) and Ceccarelli et al. (1996) on a log-log scale, so power-law distributions become straight lines and the outer regions of the envelope stand out more clearly. Our profiles agree well with those of Schöier et al. (2002) who derived the density and temperature profiles independently from a subset of our continuum measurements. Our values for the infall parameters compare well with those derived by Schöier et al. ( $a = 0.65 - 0.95 \text{ km s}^{-1}$ ,  $t = (1.5-3.5) \times 10^4 \text{ yr}$ ) and Ceccarelli et al. ( $a = 0.5$ ,  $t = 2.3 \times 10^4 \text{ yr}$ ). The age is more than a factor of two lower than derived by Narayanan et al. (1998). This is probably because our study is focused on high- $J$  transitions, and therefore more sensitive to the warm inner envelope regions, while previous work dealt mostly with lower  $J$  transitions which are dominated by the gas in the colder outer envelope regions.

We used the azimuthally averaged radial emission profile (Fig. 4) to determine independently the infall parameters from the SCUBA continuum maps. A best fit of the inside-out collapse model from Shu (1977) yields a sound speed  $a = 0.7 \text{ km s}^{-1}$  and an age  $t = (0.6-2) \times 10^4 \text{ yr}$ , close to the values derived from our fits to the line profiles. This indicates that the model of Shu can be used to predict the infall velocities for this class of YSOs, but that the age is better constrained from the line profiles. Schöier et al. (2002) also found a discrepancy between the infall parameters derived from dust continuum and molecular line emission. The infall analysis of Hogerheijde & Sandell (2000) for a sample of YSO envelopes indicate that this discrepancy may be a common property of Class 0 YSOs, since a better correspondence was found for Class I and older sources. A possible explanation is that collapse models generally predict a much higher mass-accretion rate early in the evolutionary stage than the Shu model does. We therefore use the infall parameters  $a$  and  $t$  from the  $\text{DCO}^+$  fit to model the profiles of the observed molecular lines and to infer the abundances, the results are presented below.

### *HDO*

The best fit to the observed HDO profile implies a constant abundance of  $3 \times 10^{-10}$  throughout the envelope. The model profile is narrower than observed. This may indicate a significant contribution to HDO emission from, e.g., the outflow(s) (§4.3). To reproduce the line wings by infall, the sound speed must increase to  $a = 1 \text{ km s}^{-1}$ . The fit to the absorption could be improved by adding a cold shell with  $T < 10 \text{ K}$ . But, HDO collision rates are only available for  $T \geq 50 \text{ K}$  (Green 1989). Our models use the 50 K rates at lower temperatures while the true rates may easily be a factor of two lower at  $T \simeq 12-15 \text{ K}$  enhancing the optical depth of the HDO line. We therefore expect that extended collision rates would improve the fit

of the line profile. The continuum level results from the included FIR radiation field in the excitation analysis and matches the observed level very well (Fig. 8).

We use the best HDO infall model fits ( $a = 1 \text{ km s}^{-1}$ ,  $t = 2.5 \times 10^4 \text{ yr}$ ) to model the HDO  $2_{11}-2_{12}$  and  $3_{12}-2_{12}$  lines. These lines have energy levels far above ground and are not expected to be collisionally excited for this temperature range. However, in high mass YSOs these lines are found to be much stronger than expected on basis of collisional excitation (Jacq et al. 1990; Helmich et al. 1996b; Gensheimer et al. 1996), probably because the high levels are populated through excitation by the FIR radiation field. With the earlier mentioned dust parameters for the FIR excitation, the model yields a  $2_{11}-2_{12}$  peak intensity of  $T_{\text{R}}^* = 0.006 \text{ K}$ , and  $3_{12}-2_{12} T_{\text{R}}^* = 0.001 \text{ K}$ . The former value is much lower than the upper limit to the line strength of 0.08 K from van Dishoeck et al. (1995) for the  $2_{11}-2_{12}$  line. Since the upper-limits of van Dishoeck et al. for the  $2_{11}-2_{12}$  and  $3_{12}-2_{12}$  lines are high with respect to what can be achieved with present-day, more sensitive receivers, we decided to reobserve both lines. Deep spectra reveal no features at a noise rms of 0.02 K at either frequency for a spectral resolution of 1.25 MHz ( $=1.7 \text{ km s}^{-1}$ ).

## $H_2O$

The excitation of  $H_2O$  has been calculated using the collision rates of ortho- and para- $H_2$  with ortho- $H_2O$  (Phillips, Maluendes & Green 1996) for kinetic temperatures between 20 and 140 K for the lowest 5 rotational energy levels of  $H_2O$ . This range traces the temperature structure of our model very well. We interpolated the rates for the appropriate temperature of each shell. The ortho/para  $H_2$  ratio in each shell is assumed to be in LTE at the appropriate temperature of each shell; for low temperatures,  $T_{\text{kin}} < 70 \text{ K}$ , most of the  $H_2$  is in its para modification and  $[\text{ortho-}H_2]/[\text{para-}H_2] \rightarrow 0$  for lower  $T_{\text{kin}}$ .

We included FIR dust excitation in our model, using the dust emissivities from Ossenkopf & Henning (1994). Calculations with a large range in power-law emissivities show that the dust emission has not much impact on the excitation of the lowest water lines in the envelope of I16293A. Therefore, we did not consider the FIR radiation in our further calculations. The total  $H_2O$  abundance is derived assuming an ortho-to-para  $H_2O$  ratio of 3 : 1.

The abundance was varied to fit the self-reversal and to match the  $1_{10}-1_{01}$  peak  $H_2O$  emission observed by SWAS. Our infall models fail to match the large width of the observed  $H_2O$  spectrum. This is not surprising; in the large SWAS beam (FWHM  $\simeq 4 \text{ arcmin} \simeq 35,000 \text{ AU}$ ) emission from our model cloud is dominated by the cold outer envelope. The width of the observed line profile clearly indicates that most of the  $H_2O$  emission arises in molecular

outflows associated with this Class 0 YSO which are not included in our envelope model. We therefore focus here on the region causing the absorption and the emission at the systemic velocity of the cloud, and model the H<sub>2</sub>O outflow in §4.3. Our envelope model predicts a narrow double-peaked profile which can match the intensity level of the observed maxima, but not the width (Fig. 10). Initially, the analysis was done for a uniform abundance [ortho-H<sub>2</sub>O]/[H<sub>2</sub>]=2 × 10<sup>-7</sup> across the envelope. This fits the maximum emission, but causes too deep an absorption. To reduce the absorption we applied a step function for the abundance profile with a drop in the H<sub>2</sub>O abundance at  $T_{\text{kin}} = 14$  K, where atomic oxygen starts to freeze out. Such a two-step abundance profile fits the observations for [ortho-H<sub>2</sub>O]/[H<sub>2</sub>]=3 × 10<sup>-9</sup> for  $T_{\text{kin}} < 14$  K (Fig. 10). The FIR H<sub>2</sub>O lines observed with ISO (Ceccarelli et al. 2000) are much stronger than predicted by our model, indicating that they do not originate in the envelope.

### $H_2D^+$

The H<sub>2</sub>D<sup>+</sup> 1<sub>10</sub>–1<sub>11</sub> line has been marginally detected at a 3-sigma level. A constant abundance of 3 × 10<sup>-10</sup> yields a good fit to the observed maximum emission, but the line width of the model spectrum is too large. We therefore tried a step function for the abundance, [H<sub>2</sub>D<sup>+</sup>]/[H<sub>2</sub>]=1 × 10<sup>-12</sup> for  $T_{\text{kin}} > 20$  K and [H<sub>2</sub>D<sup>+</sup>]/[H<sub>2</sub>]=2 × 10<sup>-9</sup> for  $T_{\text{kin}} < 20$  K which yields a good fit to the complete line profile (Fig. 8).

### $N_2H^+$

The N<sub>2</sub>H<sup>+</sup> 4–3 line was observed simultaneously with the H<sub>2</sub>D<sup>+</sup> 1<sub>10</sub>–1<sub>11</sub> line. A constant abundance with the radius of 3 × 10<sup>-11</sup> yields a good fit to the observed line profile (Fig. 8).

### $HCO^+$

We can only put a lower limit to the HCO<sup>+</sup> abundance of 1 × 10<sup>-9</sup>, where the line 4–3 starts to become optically thick. However, this does not match the peak intensities well, nor does it fit the apparent extra blue and red components. The wings are well matched for  $a = 1$  km s<sup>-1</sup>. An outflow is likely contributing to the emission. The abundance for  $T_{\text{kin}} < 10$  K could be enhanced to get a deeper absorption, but this would not add much information since the emission and the absorption are already optically thick. Note that the high optical depth of the emission and absorption masks any signature of chemical changes at low temperatures. This transition is therefore not suited for an accurate derivation of the abundance structure.

$H^{13}CO^+$

For this  $HCO^+$ -isotopomer, we also have problems in modeling the observed double line structure, probably because kinematically distinct components are present at the blue side (Fig. 8). An abundance of  $2 \times 10^{-11}$  gives a good fit to the red component. This component is optically thin and we attribute it to the envelope. Note that a constant abundance throughout the envelope is used for this fit. The blue component is probably associated with one of the quadrupole outflow components (§4).

$^{12}CO$

The CO 6–5 and 7–6 lines have been modeled for a  $^{12}CO$  abundance  $[^{12}CO]/[H_2] = 1 \times 10^{-4}$ . In Fig. 11 the model spectra are overlaid on the observations. It can be seen that the envelope model fails to fit the observed emission for a sound speed  $a = 0.7 \text{ km s}^{-1}$ . Even for  $a = 1 \text{ km s}^{-1}$ , the width and maxima of the observed spectra cannot be matched. This indicates that, like the  $H_2O$  emission, most of the observed high- $J$   $^{12}CO$  emission is associated with the outflows (§4.3).

$C^{18}O$

The  $C^{18}O$  3–2 line profile can well be fitted for an abundance of  $2 \times 10^{-7}$  throughout the envelope, corresponding to a ‘standard’  $[CO]/[H_2]$  abundance of about  $10^{-4}$ . Schöier et al. (2002) derive a  $C^{18}O$  abundance of  $6.2 \times 10^{-8}$  on basis of similar observations with the JCMT. However their abundance yields a fit to the spectrum which is about a factor of two lower than our fit (see their Fig. 4), so the agreement is within a factor of 1.5. Our abundance-fit yields a  $C^{18}O$  2–1 spectrum whose central region is quite different from the observations indicating a lower abundance. The observed low emission level of the  $C^{18}O$  2–1 may be caused by a low-density  $C^{18}O$  component with a ‘standard’ abundance residing in dark/translucent transition region between the outer envelope and the diffuse interstellar medium, while CO in the cold outer envelope regions may be highly depleted. Moreover, the modeled  $C^{18}O$  2–1 and 3–2 line profiles are somewhat narrower than observed. The line wings of both transitions can be fitted by infall if a sound speed of  $a = 0.9 \text{ km s}^{-1}$  is adopted, or there may be a contribution from the outflow. Figure 8 plots the excitation model fit for the  $C^{18}O$  3–2 line. We conclude by noting that the low- $J$   $C^{18}O$  transitions are not well suited to determine the CO depletion in the envelope since the line profile indicates than  $C^{18}O$  is sensitive to material which may not reside in the envelope.

### $C^{17}O$

We use a constant  $C^{17}O$  abundance of  $4 \times 10^{-8}$ , i.e., a ‘standard’ CO abundance for  $T_{\text{kin}} > 20$  K and depletion by a factor of 50 for  $T_{\text{kin}} < 20$  K. This fits better than a uniform abundance throughout the envelope, because depletion makes the line appear broader. The line is also broadened by unresolved hyperfine lines, e.g., visible as a low-velocity shoulder. Still, the observed line is broader than our model predicts. The wings fit better for a sound speed  $a = 0.9 \text{ km s}^{-1}$ . There is a hint for a depression of the peak emission. Schöier et al. (2002) derive a  $C^{17}O$  abundance of about  $2 \times 10^{-8}$  which agrees within a factor of two with our results using a constant abundance value.

### $H_3O^+$

The ortho- $H_3O^+$   $3_0^+ - 2_0^-$  line at 396.272412 GHz has been searched for in I16293A by Phillips et al. (1992). We used their upper limit and our envelope excitation model to constrain the abundance  $[\text{ortho-}H_3O^+]/[H_2] < 1.5 \times 10^{-9}$ . This corresponds to an  $[\text{H}_3O^+]/[H_2]$  upper limit of  $(3-5) \times 10^{-9}$  if the  $H_3O^+$  resides mainly in the  $T_{\text{kin}} < 50$  K region, or  $T_{\text{kin}} > 50$  K region, where the  $[\text{ortho-}H_3O^+]:[\text{para-}H_3O^+]$  ratio varies between 1 : 2 and 1 : 1, respectively. These upper limits are about an order of magnitude larger than derived by Phillips et al. (1992) using statistical equilibrium calculations for a slab with a homogeneous density and temperature.

The derived abundances of all species are summarized in Table 3 together with those of Schöier et al. (2002). Taking into account the differences between their fits to the observed spectra and ours (see above), the abundances agree within a factor of 1.5.

## 4. The CO Outflows and What Drives Them

### 4.1. The NE–SW Flow: Powered by I16293A

The symmetry axis of the NE–SW outflow, as determined from our CO 2–1 map, goes through A at all velocities (Fig. 12). The centroid of the overlapping blue- and red-shifted emission is centered on I16293A, which is also evident from the velocity position plot in Fig. 13 (although inescapably includes some of the E–W outflow). Furthermore, aperture synthesis maps of dense outflow tracers, especially CS (Walker et al. 1993) and SO (Mundy et al. 1992) clearly show high velocity gas emanating from I16293A in the direction of the CO outflow, while I16293B shows no activity, nor does it seem to be associated with a maximum in any high density gas. We therefore attribute the NE–SW outflow to I16293A.

Our submillimeter maps (Figs. 1 and 4) clearly show that the dust emission associated with the free-free and millimeter-source I16293A is extended. This is one of the few YSOs where we can resolve the dust emission: it has a disk-like structure with a size of roughly 2000 AU. At low frequencies the continuum emission from I16293A splits up into a double source. We do not believe that I16293A is in itself a binary; a more plausible interpretation is that we are seeing highly collimated ionized gas from the outflow, as has been seen in L1551 IRS5 (Bieging et al. 1985; Rodríguez 1986), where the jet dominates the emission at low frequencies and the disk emission becomes dominant at high frequencies. These are strong arguments for an accretion disk that is centered on I16293A and drives a powerful outflow, which is very well collimated close to the star (e.g., free-free emission), but relatively highly collimated even in CO. The ratio of length to width is about 1:3 at high velocities. The outflow is at high inclination, since we can see overlap between the blue- and the red-shifted lobe. If we assume the outflow to be conical, which according to the velocity position plot (Fig. 13) appears to be a reasonable assumption, we can use the method outlined by Liseau & Sandell (1986) to estimate the inclination of the outflow, and find about  $65^\circ$  for both the blue and the red lobe. This is slightly higher than what Hirano et al. (2001) find on the basis of their SiO 2–1 map for the NE red lobe, where they derive an inclination by  $40\text{--}45^\circ$  from the plane of the sky.

The properties of the outflow have been derived in several studies (e.g., Walker et al. 1988; Mizuno et al. 1990; Castets et al. 2001; Hirano et al. 2001; Garay et al. 2002; Lis et al. 2002, but we will redo it here; partly because we have more accurate data, but also to point out how uncertain these estimates are. The deep integrations of  $^{13}\text{CO}$  and  $\text{C}^{18}\text{O}$  toward I16293A (Fig. 2) clearly show high velocity emission, which indicates that the  $^{12}\text{CO}$  optical depth in the wings is substantial. At near outflow velocities ( $\sim 1.5 \text{ km s}^{-1}$  from the cloud systemic velocity) we find optical depths of 40 or more, both from  $^{13}\text{CO}$  and  $\text{C}^{18}\text{O}$ , but note that here the line wings originate from both outflows and also get a significant contribution from the underlying accretion disk. We therefore obtained additional  $^{12}\text{CO}$  and  $^{13}\text{CO}$  spectra at the peak positions in the lobes of the NE–SW outflow, i.e., at offset positions  $(+80'', +55'')$  for the redshifted lobe and  $(-130'', -40'')$  for the blueshifted lobe. These show that the red-shifted outflow has substantially higher optical depth. We estimate a  $^{12}\text{CO}$  2–1 optical depth of about unity at radial velocities as high as  $11 \text{ km s}^{-1}$  away from the systemic velocity of the cloud, whereas the optical depth has dropped to unity at  $+6 \text{ km s}^{-1}$  away from the cloud core for gas in the blue-shifted outflow. The  $^{13}\text{CO}$  spectra are not sensitive enough to enable us to derive optical depths of less than about unity.

We compute the outflow mass, momentum, momentum flux, and energy content with and without opacity corrections, by assuming that we can apply the same opacity correction to all of the gas in the outflow. Since we have not directly measured the excitation

temperature of the outflowing gas we assume it to be 50 K, but note that it could be as high as 80 K (van Dishoeck et al. 1995). The values in Table 4 are obtained assuming an abundance ratio  $10^{-4}$  for  $[\text{CO}]/[\text{H}_2]$  and summing over the map in  $1 \text{ km s}^{-1}$  wide velocity intervals starting  $1 \text{ km s}^{-1}$  from the cloud systemic velocity (assumed to be  $4 \text{ km s}^{-1}$ ). The apparent dynamic outflow time scales are about the same for both lobes,  $(3.0\text{--}3.5)\times 10^3 \text{ yr}$ . This agrees with the dynamical timescale of  $(5\text{--}7)\times 10^3 \text{ yr}$  derived by Hirano et al. (2001) for the NE red lobe. However, the blue outflow lobe appears more energetic. Normally when one sees an imbalance in the momentum or force of the outflow, it is an indication that one of the outflow lobes has penetrated the cloud surface and therefore has no gas to interact with. Here we see no evidence for this. A more likely explanation is that we have not properly corrected for the opacity and excitation differences in the two outflow lobes. The blue lobe is more extended and has higher apparent velocities, suggesting that the gas surrounding the blue lobe is less dense than the gas surrounding the red outflow lobe. This is also seen in our opacity estimates, which are higher for the red-shifted outflow. A similar conclusion is reached by Hirano et al. (2001) and Garay et al. (2002) on basis of SiO and  $\text{CH}_3\text{OH}$  maps, respectively.

#### 4.2. The E–W Outflow: A Fossil Flow Driven by I16293B

The symmetry axis of the E–W outflow passes north of I16293A, but not as clearly defined as the NE–SW outflow. The red-shifted outflow lobe is much more compact than the blue-shifted lobe, and appears to bend more towards the north. However, the peak intensity of the outflowing red-shifted gas is rather well aligned with the large blue-shifted outflow lobe with an average position angle for the flow of  $PA \simeq 96 \pm 3^\circ$ . The E–W outflow appears to intersect with the continuum disk about  $5\text{--}10''$  north of I16293A. Since there is no source near this position other than I16293B, we associate the E–W outflow with I16293B. A similar conclusion was also drawn by Walker et al. (1993), although they stress that at present there is no evidence for outflow activity in the immediate vicinity of B. Garay et al. (2002) find that the  $\text{CH}_3\text{OH}$  wing emission has a narrow and nearly constant velocity width along the E–W lobes, which they attribute to turbulent entrainment. This is consistent with our finding that the E–W outflow is a fossilized flow.

It has been suggested that the NE red outflow lobe and the eastern blue outflow lobe could be part of a wide angle flow similar to the L 723 outflow (Walker et al. 1988) or that the two outflows are part of a precessing or episodic outflow driven by the same star (Walker et al. 1988, 1993; Mizuno et al. 1990). However, our CO map clearly shows that these are two separate outflows. Since the symmetry axis of the E–W outflow does not

intersect with I16293A, it is rather unlikely that this outflow would have been caused by an earlier outflow episode from I16293A. Hirano et al. (2001) and Garay et al. (2002) also conclude that two independent bipolar outflows are present on the basis of their SiO and CH<sub>3</sub>OH maps. Mizuno et al. (1990) also discuss a third outflow, because in their low spatial resolution Nagoya map, the E–W outflow extends more than 10' from IRAS 16293–2422 and their high resolution Nobeyama map does not show this extended outflow component. Our map does not extend as far as the Nagoya map, and our spatial resolution is poorer than that of the Nobeyama CO 1–0 map. However, the CO map we present here has the advantage of being fully sampled, unlike the SiO 2–1 emission mapped by Hirano et al. (2001), and it has a much higher resolution (20'') than the large-scale SiO 2–1 map of Garay et al. (2002) (57''). We therefore better resolve the two outflows. One can clearly see that the outflow continues to the east outside the area we have mapped, but with rather low velocities. Therefore the extended blue low-velocity outflow appears simply a continuation of the E–W flow.

We also clearly see the interaction of this outflow with the I16293E core, which was already found by Mizuno et al. (1990). In our channel maps, which are overlayed on the 800  $\mu$ m-continuum emission (Fig. 12), this interaction is clearly visible. It appears rather gentle: the outflow is enhanced at low velocities and seems to stream around the core and forms almost a cavity immediately behind it. That it streams around the core region is supported by the fact that we see faint red-shifted <sup>12</sup>CO towards the dense core region, but the red-shifted emission is much stronger in front of the core, although one can still see it faintly on the backside as well (Fig. 12). Figure 5 shows a blow-up of the 450  $\mu$ m image of I16293E. It is clear that the outflow has compressed the core and caused the high density N–S ridge that we see in our continuum maps and prominently at near cloud velocities in the channel-maps of Fig. 12. Behind the core it appears that the outflow gets recollimated. There is no indication of interaction between I16293E and the red-shifted NE outflow lobe from our CO channel maps, nor from the SiO channel maps (Hirano et al. 2001; Castets et al. 2001; Garay et al. 2002). Castets et al. (2001) attribute the blue and red stream of the E–W outflow around the I16293E core to the red and blue lobe of an outflow powered by I16293E causing two shocked regions (HE1 and E1 in their nomenclature) visible in their H<sub>2</sub>CO maps. They support their hypothesis by means of HCO<sup>+</sup> 1–0 spectra taken along a slice which goes through I16293E as well as through the peaks in the H<sub>2</sub>CO emission, since these spectra reveal a blue wing at one side of I16293E and a red wing on the counter side. Although these wings are real, the results are different when put in context of the entire cloud. Our large maps show what small maps, which do not fully cover the complete interaction region of the extended outflows with the LDN 1689N cloud, cannot: local small scale flows in the vicinity of I16293E are part of large scale motions. From our CO map it is clear that the apparent SW–NE outflow and the alignment with I16293E are due to projection effects of

pieces of the E–W outflow from I16293B which streams around the dense prestellar core I16293E. This view is supported by the study of Hirano et al. (2001) who find that the E–W flow has fan-shaped lobes, each of which containing blue- and red-shifted components. This would imply that E1 is red-shifted gas in the far side of the eastern blue lobe. The red-shifted shocked region E1 is thus the interaction region of the E–W outflow, while the blue-shifted H<sub>2</sub>CO peaks HE1 and HE2 from Castets et al. (2001) are the interaction of the near side of the E–W blue lobe with dense gas of LDN 1689N located at the southwest and southeast side of the dense core I16293E. These interaction regions could also be the edges of I16293E.

### 4.3. The High-*J* CO, HDO, and H<sub>2</sub>O Emission: Outflow Modeling

Section 3.2.3 found that the envelope model of I16293A can reproduce the line profiles of most observed molecular transitions, but not of CO 6–5 and 7–6, HDO, and H<sub>2</sub>O. Although the absorption at the cloud systemic velocity can be fit with an envelope model, the broad emission cannot be reproduced even for sound speeds as high as  $a = 1 \text{ km s}^{-1}$ . Here we investigate the origin of the broad high-*J* CO, HDO, and H<sub>2</sub>O wings by means of an outflow model.

We have scaled our CO 7–6 emission to the level of the H<sub>2</sub>O emission (Fig. 14). It is striking that the two spectra have such a similar shape despite the fact that the beam sizes differ by a factor of about 30. The match of the absorption widths is also very good, and indicates that we may see here the same region with JCMT and SWAS in absorption. In addition, the line wings are similar, although at the blue side there is an extra CO emission component while at the red side there is an extra H<sub>2</sub>O emission component present. But the extent of the wings is similar for both species. Does this mean that the wings are from a very small region covered by both beams, or that the wing component is rather uniformly distributed throughout the cloud?

The SWAS data were fitted with a Monte Carlo radiative transfer code and a physical model of a spherically symmetric cloud subdivided into shells of constant physical conditions. The use of the code and its application to water lines is described in Ashby et al. (2000), which also analyzes the variety of water line profiles and establishes broad diagnostics of outflow, infall, and turbulence apparent in SWAS data. The line shape lead us to explore models which combine outflow and turbulence; we find that the line strengths depend on the velocity field as well as on the temperature and abundance in a complex relation. Figure 10 (middle panel) shows the predicted ortho-H<sub>2</sub>O spectra from the outflow model with an ortho-H<sub>2</sub>O abundance of  $1 \times 10^{-8}$  throughout, a turbulent velocity of  $2.3 \text{ km s}^{-1}$ , and maximum outflow velocity  $V = 5.8 \text{ km s}^{-1}$ . The temperature ranges from 200 K to 15.5 K. The outflow

model provides an acceptable fit to the observed extended wing emission, but cannot explain the central part of the observed profile. The outflow model results are complementary to the infall modeling of the ortho-H<sub>2</sub>O line (Fig. 10, top and middle panel), which fits only the central region of the observed spectrum. To illustrate this qualitatively, we plotted in Fig. 10 (bottom panel) the sum of the outflow and envelope spectra of ortho-H<sub>2</sub>O which indeed yields a rather good description of the entire SWAS spectrum. Note that the red wing of the H<sub>2</sub>O emission is not fitted by our model, this may be due to multiple outflows (§4.1 and §4.2) which we did not model. For a quantitative comparison we do not only need a multiple outflow model but also have to incorporate the outflow and infall models in one single excitation model since they overlap in extent and velocity space. This could mean that part of the blue infall gets absorbed by the blue outflow component and vice versa. An avenue for further study would be a combined infall and outflow model.

The same outflow models were used to model the CO 6–5 and 7–6 lines in the JCMT beam using an abundance  $[\text{CO}]/[\text{H}_2]=10^{-4}$  (Fig. 11). The wing emission predicted by the outflow model poorly fits the observed emission which indicates the presence of multiple outflows, analogous to the H<sub>2</sub>O situation.

Finally, we calculated the HDO emission in the outflow in a 11" beam. We started with a uniform  $[\text{HDO}]/[\text{H}_2]$  abundance of  $3 \times 10^{-10}$ , similar to the envelope value. This yields a spectrum which matches the maximum intensity of the observed emission, but not the wings (Fig. 15). This may be due to the presence of multiple outflows, similar to the H<sub>2</sub>O case. The outer wings can be fitted for an abundance of  $3 \times 10^{-9}$  and results in a self-reversed profile, but its peak intensity is too high by a factor of 2–4. This is not surprising since we do not include an infalling envelope. A better fit may be obtained by a combined (multiple) outflow and infall model as discussed above for H<sub>2</sub>O. We conclude that our shock model can explain the wings of the observed HDO emission and that the HDO abundance in the outflow may be somewhere in the range from  $3 \times 10^{-10}$  to  $3 \times 10^{-9}$ .

## 5. The $[\text{HDO}]/[\text{H}_2\text{O}]$ Abundance Ratio Structure Toward I16293A

### 5.1. Derived $[\text{HDO}]/[\text{H}_2\text{O}]$ Profile From Envelope Excitation Analysis

It is clear that great caution should be taken when comparing the H<sub>2</sub>O abundance derived from the SWAS measurements and the HDO abundance derived from the JCMT observations. Nevertheless we are able to use the same models since we convolve the emerging emission with the appropriate beam. Because of the large beamsize, SWAS is not sensitive to the H<sub>2</sub>O emission from the warm inner envelope. To test this we enhanced the abundance of

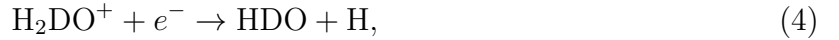
$\text{H}_2\text{O}$  for  $T_{\text{kin}} > 90$  K to the value of  $10^{-4}$ . This was not found to have any significant impact on the emission in the SWAS beam. Clearly SWAS is mostly sensitive to  $\text{H}_2\text{O}$  emission from extended colder gas in the outflow, and to a lesser extent to gas in the outer envelope region (§4.3).

The shocks associated with the outflows are able to release  $\text{H}_2\text{O}$  from the grains and effectively convert oxygen into  $\text{H}_2\text{O}$  through neutral-neutral reactions, but the velocities are so small that  $\text{H}_2\text{O}$  formation at an  $1 \times 10^{-4}$  abundance level is inhibited. Indeed, ISO LWS observations yield much lower  $\text{H}_2\text{O}$  abundances. The ISO observations of  $\text{H}_2\text{O}$  are all from higher level transitions  $E/k > 100$  K, and thus trace the hot/warm disk/core region of small extent. Ceccarelli et al. (2000) derive an  $[\text{H}_2\text{O}]/[\text{H}_2]$  abundance in the ‘outer envelope’ ( $r \geq 150$  AU) of about  $2.5 \times 10^{-7}$  which is similar to our envelope abundance ( $2 \times 10^{-7}$ ), while for the inner region ( $r \leq 150$  AU) they derive an enhanced abundance of  $1.5 \times 10^{-6}$  which is attributed to evaporation of water ice mantles of grains at  $T_{\text{kin}} \simeq 100$  K. The latter value is higher than our inferred outflow abundance of about  $10^{-8}$  (§4.3).

If we combine the  $\text{H}_2\text{O}$  abundances of Ceccarelli et al. (2000) with our derived HDO abundances we find that the  $[\text{HDO}]/[\text{H}_2\text{O}]$  abundance ratio varies between  $2 \times 10^{-4}$  in the warm envelope,  $r < 150$  AU,  $10^{-3}$  in the envelope with  $r > 150$  AU and  $T_{\text{kin}} > 14$  K, and  $8 \times 10^{-2}$  in the outer envelope where  $T_{\text{kin}} < 14$  K. For a detailed comparison between the HDO and  $\text{H}_2\text{O}$  abundances throughout the envelope we consider in the next section the temperature effects of ion-molecule chemistry and the effects of depletion of molecules and atoms which play a vital role in the formation of HDO and  $\text{H}_2\text{O}$ .

## 5.2. A Simple Chemical Model

In ion-molecule chemistry (e.g., Pineau des Forêts et al. 1989; Millar et al. 1991) HDO is thought to be formed through the dissociative recombination



with a statistical branching ratio of  $\frac{2}{3}$  compared to the corresponding recombination of  $\text{H}_3\text{O}^+$ . In steady state the gas-phase density of  $\text{H}_2\text{DO}^+$  can be written as

$$n(\text{H}_2\text{DO}^+) = \frac{(n(\text{O})k_1 + n(\text{H}_2\text{O})k_2)n(\text{H}_2\text{D}^+) + n(\text{H}_2\text{O})n(\text{DCO}^+)k_3}{n(e)k_4}, \quad (5)$$

where  $k_i$  are the relevant reaction rate coefficients. We adopt equal total rate coefficients for the reactions involving the deuterated and hydrogenated species and assume statistical branching ratios.  $\text{H}_3\text{O}^+$  is formed through similar reactions with hydrogenated species. We

will neglect the formation of  $\text{H}_3\text{O}^+$  from channels leaving the  $\text{H}_2\text{DO}^+$  reaction sequence and vice versa, and neglect the formation of  $\text{H}_3\text{O}^+$  and  $\text{H}_2\text{DO}^+$  from reactions of  $\text{H}_3^+$  or  $\text{H}_2\text{D}^+$  with  $\text{HCO}^+$ , and  $\text{DCO}^+$ , respectively. The  $[\text{HDO}]/[\text{H}_2\text{O}]$  abundance can then be written

$$\frac{x(\text{HDO})}{x(\text{H}_2\text{O})} = \frac{2}{3} \frac{x(\text{H}_2\text{DO}^+)}{x(\text{H}_3\text{O}^+)} \quad (6)$$

$$\simeq \frac{1}{18} \frac{x(\text{H}_2\text{D}^+)}{x(\text{H}_3^+)}. \quad (7)$$

The heart of the fractionation of deuterated molecules is the molecular-ion  $\text{H}_2\text{D}^+$  which is formed through reaction (1). In equilibrium the formation and destruction rates of  $\text{H}_2\text{D}^+$  are balanced which leads to (Stark et al. 1999)

$$\frac{x(\text{H}_2\text{D}^+)}{x(\text{H}_3^+)} = \frac{x(\text{HD})k_f + x(\text{D})k_D}{x(e)k_e + \sum k_i x(\text{X}) + k_r}, \quad (8)$$

where  $k_e$  is the dissociative recombination rate coefficient of  $\text{H}_2\text{D}^+$ ,  $k_D$  is the rate coefficient for the formation of  $\text{H}_2\text{D}^+$  via the reaction  $\text{H}_3^+ + \text{D}$ ,  $x(\text{X})$  is the fractional abundance of species  $\text{X}=\text{CO}$ ,  $\text{O}$ ,  $\text{H}_2\text{O}$ , etc., and  $k_f$  and  $k_r$  are the forward and backward rate coefficients of reaction (1), see Stark et al. (1999) for references of the adopted rate coefficients. The  $\text{H}_3^+$  density depends on the effective cosmic ray ionization rate  $\zeta_{\text{eff}}$  and can be written as (Lepp et al. 1987)

$$n(\text{H}_3^+) = \frac{\zeta_{\text{eff}}}{\sum k_i x(\text{X})}. \quad (9)$$

We consider only the destruction of  $\text{H}_2\text{D}^+$  through reactions with CO, assume  $x(\text{HD}) = 10x(\text{D}) = 2.8 \times 10^{-5}$ , and  $\zeta_{\text{eff}} = 5 \times 10^{-17} \text{ s}^{-1}$ . Together with the balance for  $\text{H}_3^+$  formation and destruction (Eq.[9]) we derive an expression for the  $\text{H}_2\text{D}^+$  abundance with the CO abundance as the only free parameter. This abundance structure was subsequently used as input in the excitation calculations to compute the spectrum of the ortho- $\text{H}_2\text{D}^+$  ground-state transition. A good fit to the observed  $\text{H}_2\text{D}^+$  spectrum is established for a two step CO abundance profile with  $[\text{CO}]/[\text{H}_2] = 1.5 \times 10^{-4}$  for  $T_{\text{kin}} > 22 \text{ K}$  and  $3 \times 10^{-6}$  for  $T_{\text{kin}} < 22 \text{ K}$  (Fig. 16) applied to the infall envelope model. This indicates a CO-depletion by a factor of 50 at temperatures below 22 K, where CO is frozen out. This value equals the depletion derived from our  $\text{C}^{17}\text{O}$  2–1 excitation analysis, but is a factor of 50 larger than derived from our  $\text{C}^{18}\text{O}$  2–1 and 3–2 observations which indicated no depletion (§3.2.3). However, the spectra of the latter transitions are biased toward the warm inner regions and the outflow.

Now we can use the  $[\text{H}_2\text{D}^+]/[\text{H}_3^+]$ -model fit, together with the  $\text{H}_2\text{O}$  abundances from the excitation analysis and the expression of the  $[\text{HDO}]/[\text{H}_2\text{O}]$  ratio (Eq. [7]) to determine

an HDO model abundance profile and to calculate a model spectrum analogous to  $\text{H}_2\text{D}^+$ . The model spectra are shown in Fig. 16. When we adjust  $[\text{H}_2\text{O}]/[\text{H}_2]=1.25 \times 10^{-7}$  for  $T_{\text{kin}} > 14 \text{ K}$  and  $2 \times 10^{-9}$  for  $T_{\text{kin}} < 14 \text{ K}$  we get a fit to the observed emission peaks. Note that these abundances agree within the uncertainties with the derived  $\text{H}_2\text{O}$  excitation results. The HDO chemistry model spectrum (Fig. 16) resembles the HDO excitation infall spectrum (Fig. 8) very well. The fact that the absorption does not go down to zero is a result of the uncertainty in the HDO collision rates for  $T_{\text{kin}} < 50 \text{ K}$ . Note that the HDO spectrum is calculated self-consistently from the theoretical  $[\text{HDO}]/[\text{H}_2\text{O}]$  expression and the  $\text{H}_2\text{O}$  2-value abundance profile from the excitation analysis, i.e., it does not provide an independently determined HDO abundance structure.

### 5.2.1. *Observational Results Versus Chemistry Models*

The upper-limits on the ortho- $\text{H}_3\text{O}^+$  abundances derived from the observations by Phillips et al. (1992) in §3.2.3 can be used to determine an upper limit to the  $\text{H}_2\text{O}$  abundance. From the formation and destruction balance of  $\text{H}_2\text{O}$ , we derive  $[\text{H}_2\text{O}]/[\text{H}_3\text{O}^+] \simeq 1000\text{--}1500$  where we used the experimentally determined branching ratio of 0.5 from Jensen et al. (2000) to form  $\text{H}_2\text{O}$  in the dissociative recombination of  $\text{H}_3\text{O}^+$ . Furthermore we only considered the formation of  $\text{H}_2\text{O}$  via the  $\text{H}_3^+$  channel and assume that 10% of all ions cause destructive dissociation of  $\text{H}_3\text{O}^+$ , similar to Phillips et al. (1992). The upper- and lower-limits correspond to the  $T_{\text{kin}} \leq 50 \text{ K}$  and  $T_{\text{kin}} = 80 \text{ K}$  ranges, respectively. The observations then yield  $[\text{H}_2\text{O}]/[\text{H}_2] < 5 \times 10^{-6}$  for both temperature ranges and are consistent with the abundances derived by Ceccarelli et al. (2000) from ISO observations.

The derived  $\text{H}_2\text{O}$  abundance in the outflow is  $1.3 \times 10^{-8}$  and agrees with the dynamical/chemical model of Bergin et al. (1999) for a pre-shock chemistry which evolves until  $t = 10^3 \text{ yr}$ . The same model predicts significant deuterium fractionation in the pre-shock gas after  $10^6 \text{ yr}$ :  $[\text{HDO}]/[\text{H}_2\text{O}] \sim 10^{-3}$ , in agreement with our derived value for the envelope region where  $r > 150 \text{ AU}$  and  $T_{\text{kin}} > 14 \text{ K}$ . For the warm inner-envelope region  $r < 150 \text{ AU}$ , we derive  $[\text{HDO}]/[\text{H}_2\text{O}] = 2 \times 10^{-4}$ . Our gas-phase chemistry model predicts values about two orders of magnitude lower for this region. We attribute the observed enhancement to the shock induced release of solid water (HDO,  $\text{H}_2\text{O}$ ) from the grains.

### 5.2.2. $[HDO]/[H_2O]$ in the Cycle of Star- and Planet Formation

Our derived  $[HDO]/[H_2O]$  ratio in the cold ( $T_{\text{kin}} < 14$  K) envelope regions is 0.08. This ratio is however an upper limit due to the fact that the HDO collision rates are only available for  $T_{\text{kin}} \geq 50$  K. For lower temperatures we used the 50 K values, but the rates are expected to decrease for lower temperatures, so that the true HDO abundance may be lower than we derived in §4. Since oxygen starts to freeze out at  $T_{\text{kin}} = 14$  K we may also expect a drop in HDO which is similar to  $H_2O$  (§5.2. Thus, the  $[HDO]/[H_2O]$  ratio may be in the range  $10^{-3}$ – $8 \times 10^{-2}$  at  $T_{\text{kin}} < 14$  K. The  $[HDO]/[H_2O]$  chemistry model (Eq. [7]) reaches a maximum value of  $\sim 0.06$  when  $[H_2D^+]/[H_3^+] \rightarrow 1$ . Thus, the observed  $[HDO]/[H_2O]$  ratios can be understood from pure gas-phase deuterium chemistry at low temperatures.

The  $[HDO]/[H_2O]$  abundance ratio in the warm inner-envelope ( $2 \times 10^{-4}$ ) of I16293A is close to the value that has been measured in the solar system:  $3.0 \times 10^{-4}$  in the comets Hale-Bopp, Halley, & Hyakutake (Eberhardt et al. 1995; Bockelée-Morvan et al. 1998; Meier et al. 1998), and  $1.5 \times 10^{-4}$  in the Earth’s oceans (Lécuyer et al. 1998). These values are all so close as to suggest that the  $[HDO]/[H_2O]$  abundance ratio may be a constant in the cycle of star- and planet formation. The fundamental question is then: where and when is the  $[HDO]/[H_2O]$  ratio determined? There are currently two favoured scenarios (e.g., Aikawa & Herbst 1999; Aikawa et al. 2001): 1) deuteration from ion-molecule chemistry in the protoplanetary disk; 2) deuteration determined by gas phase and/or solid state chemistry in the dense interstellar medium, namely in the parent molecular cloud before star formation begins. Aikawa et al. (2002) modeled the  $[HDO]/[H_2O]$  ratio in accretion disks models and found values of the order of  $10^{-3}$  for  $R > 100$  AU in the cold midplane where  $T_{\text{kin}} \simeq 15$  K. This may indicate a large depletion of  $H_2O$  while HDO is still in the gas phase. Unfortunately the JCMT and SWAS observations cannot be used to determine the (deuterated) water abundances in the circumstellar disk. For the moment we can only make a comparison for the HDO abundance in the warm envelope. Our derived  $[HDO]/[H_2]$  abundance ratio of  $3 \times 10^{-10}$  is comparable within a factor of a few to the protoplanetary disk model of Aikawa et al. (2002) with mass accretion rate  $10^{-9} M_\odot \text{ yr}^{-1}$ , and supports the hypothesis that the HDO abundance in the disk and warm envelope are equal.

## 6. The nature of I16293A, B and I16293E

### 6.1. I16293A

I16293A is a Class 0 source, i.e., is believed to be a protostar according to the classification proposed by André et al. (1993). It is invisible in the near- and the mid-infrared,

it is associated with free-free emission so it has already formed a stellar-like core, it drives a powerful molecular outflow, and it is surrounded by an envelope of dust and gas. Even though the temperature that we derive for the dust disk surrounding I16293A is higher than the canonical value of 30 K proposed by André et al. (1993), the ratio of submillimeter to bolometric luminosity is typical for Class 0 sources, namely  $> 5 \times 10^{-3}$ . For I16293A we derive  $L_{\text{submm}}/L_{\text{bol}} \geq 2 \times 10^{-2}$ . Note that this is really a lower limit, since our estimate for the bolometric luminosity also includes the luminosity of I16293B, which is likely to be a few  $L_{\odot}$ , while its contribution to the submillimeter luminosity is negligible. Bontemps et al. (1996), in their study of outflow properties of a sample of Class I and Class 0 sources, find that Class 0 sources in general have a much higher outflow efficiency (defined as the ratio of momentum flux to radiative force) than Class I sources, with an average ratio for Class 0 sources of about 1000. For the I16293A outflow we find  $F_{\text{CO}}/F_{\text{rad}} \sim 730$ , which is close to the average value found by Bontemps et al. (1996). They also included I16293A in their sample, but the outflow momentum they derive is significantly larger because they also include the E–W outflow, which is driven by I16293B.

## 6.2. I16293B

Although it is most likely that I16293A and I16293B originate from the same collapsing core, I16293B remains much more of an enigma. Our observations support the suggestion of Walker et al. (1993) that I16293B drives the large E–W outflow. Our observations also show that the submillimeter dust emission peaks on I16293A and more or less follows the  $\text{C}^{18}\text{O}$  emission mapped by Mundy et al. (1990). Single dish observations have insufficient resolution to show any contribution from I16293B at all, even though we know from VLA and 3 mm aperture synthesis studies (e.g., Mundy et al. 1992) that the spectral index of I16293B is much steeper than that of I16293A and indicative of dust emission.

What is I16293B? Based on the scarce evidence that we have, I16293B looks like a young T Tauri star, which has driven an extremely powerful large outflow which extends  $\sim 0.45$  pc on the blue-shifted side. Such outflows from low-luminosity young stars are not uncommon; they are seen both as large scale optical jets (Bally & Devine 1997) and large scale CO outflows (Padman et al. 1997). I16293B is a low-luminosity star,  $< 5 L_{\odot}$ , associated with compact dust emission; the true luminosity may be found by means of high resolution millimeter-wave observations.

### 6.3. I16293E

We derive a bolometric luminosity  $L_{\text{bol}} = 2.3 \text{ L}_{\odot}$  for the prestellar core I16293E, and find that its FIR continuum spectrum resembles that of the Class 0 source I16293A (Fig. 4). Castets et al. (2001) quote a dust temperature  $T_{\text{d}} = 24 \text{ K}$  for this source, higher than our value of  $T_{\text{d}} = 16 \text{ K}$  since we correct for the overlapping envelope of I16293A at the position of I16293E. This correction is important since both cores are connected with a bridge-like structure (Figs. 1, 5).

The temperature and density structure of I16293E resembles the conditions in the outer envelope of I16293A. It is very interesting that the HDO abundance of the warm envelope of the YSO, and the core of I16293E are similar. This suggests that some of the gas species in the warm envelope may still have the abundance that they had in the prestellar stage, the difference being that the gas in the warm envelope is excited and thus easier to detect. A comparison between I16293E and I16293A could therefore be very important to understand the formation of a first hydrostatic core, a so-called Class –I protostar (Boss & Yorke 1995). Such protostars lie between the prestellar clouds and the Class 0 protostars, and occur when a collapsing cloud first becomes optically thick, heats up and reaches a quasi continuum stage. This stage is short lived, about  $2 \times 10^4 \text{ yrs}$ , after which a second collapse takes place and the final protostar is formed. Class –I protostars are characterized by a central core of about 200 K, embedded in a cold core of about 10 K, although the models of Boss & Yorke mostly reached a central source with a much lower temperature of 20 K.

Is a first protostar present in I16293E? Most of the observed molecular line profiles from I16293E show two peaks with a stronger redshifted peak, characteristic of expansion motions. In §4.2 we argue that this may be due to projection effects of pieces of the E–W outflow from I16293B which streams around I16293E. We also do not find an outflow associated with I16293E in our CO maps (§4.2), so it should be younger than a Class 0 object. A central Class –I protostar with  $T_{\text{kin}} = 20\text{--}200 \text{ K}$  may be present but very hard to detect in deep mid- or far infrared continuum imaging since the spectral signature will be only a weak shoulder at the Wien side of the energy spectrum of the core. Such a first protostar will be very compact and have little mass,  $M_1 \leq 0.04 \text{ M}_{\odot}$ , which can easily be hidden in the dense cold I16293E core. Detection with SCUBA seems impossible because of the beam size and because the outer envelope of such a cold core will be warmer due to the interstellar radiation field and will dominate the continuum emission. Our HDO emission, which we think comes from the heart of the core, has a narrow linewidth ( $\Delta V = 0.6 \text{ km s}^{-1}$ ) and our models yield a kinetic temperature of about 16 K. This indicates that a first protostar must still be rather cold at the low end of the temperature interval of Boss & Yorke (1995). Sensitive high resolution submillimeter interferometry of the continuum with, e.g., the Atacama Large

Millimeter Array may reveal a cold accretion disk.

#### 6.4. The Extreme Deuteration of LDN 1689N

We think that LDN 1689N is a remarkable low-mass star-forming region, but not because it ‘harbors a young protostar, two molecular outflows and a cold nearby molecular core’ (Lis et al. 2002). Multiple outflows are common around YSOs and have been reported, e.g., in L1448 (Barsony et al. 1998; Wolf-Chase et al. 2000), HH 24 (Eislöffel & Mundt. 1997), and NGC 1333 (Knee & Sandell 2000). Deep studies of embedded YSOs in low-mass cores revealed the presence of apparently starless cold companion cores with masses of about a few  $M_{\odot}$  (Motte et al. 1998; Hogerheijde & Sandell 2000; Shirley et al. 2000). Strong deuteration is expected in cold dense prestellar cores which are on the verge of forming a first hydrostatic core because of the extreme depletion of molecules like CO which may result in an abundance ratio  $[\text{H}_2\text{D}^+]/[\text{H}_3^+] > 1$  and a boost of the  $[\text{D}]/[\text{H}]$  ratio in molecules (§1). Indeed, several prestellar clouds have now been found to have a large depletion of CO (e.g., L1544, Caselli et al. 2002; L68, Bergin et al. 2002) and a large  $\text{H}_2\text{D}^+$  abundance (Caselli et al. 2003). But, what really is remarkable in LDN 1689N is that it can be considered as a ‘deuteration candle’ with the strongest deuteration known so-far in low-mass YSOs. What causes the extreme deuteration in the envelope of I16923A and the core of I16293E? The answer may lie in the fact that I16293AB is a binary system where the YSOs and their outflows differ in age. I16293B is probably the oldest of the two YSOs and the source of the fossilized E–W outflow (§4.2). This outflow is responsible for the dynamical interaction of a part of the eastern blue lobe with a dense dark core, the precursor of I16293E. This interaction caused a shock with velocity  $V_s = 8\text{--}10 \text{ km s}^{-1}$  (Lis et al. 2002) as measured at the deuterium peak D north of I16293E and possibly higher at the first place of impact west of the core. This could have released deuterated species which were condensed on the dust grains, and compressed the gas, which then cools efficiently to low temperature (Lis et al. 2002). Since the E–W outflow causes a less energetic shock than the NE–SW outflow (Lis et al. 2002; Garay et al. 2002) and SiO emission is found only associated with the NE–SW outflow (e.g., Garay et al. 2002), we expect only deuterated species to desorb since these were frozen out relatively late and thus are located near the outer surface of the grain mantles. These slow shocks of the outflow leave the grains mostly intact, with a post shock composition like that of a grain in a  $T_{\text{kin}} = 20 \text{ K}$  gas. The release of deuterated species, combined with the gas-phase deuterium chemistry at low temperatures, boosts the deuterium enrichment to extremely high values just after the passage of a shock; these deuterated species freeze out again in about  $10^4$  yrs.

Compression from this shock resulted in an elongated N–S structure, visible in the 450

$\mu\text{m}$  image (Fig. 5). At the north side this filamentary structure bends to the northeast where the gentle flow passes around the core; here the deuterium peak is located. This shock would cause a blue-shift of the systemic velocity in I16293E with respect to the parental LDN 1689N cloud. Indeed, the HDO spectrum toward I16293E is blue-shifted by about  $0.3 \text{ km s}^{-1}$  with respect to the systemic velocity of the LDN 1689N envelope toward I16293A (Table 1). Lis et al. (2002) also found such a blue-shift of deuterated molecules toward the deuterium peak D which is located about 10 arcsec northwest of the continuum peak of I16293E. We believe that at this position the shock has the greatest chemical impact.

This strong deuterated core may have been shocked again at a later time by the NE–SW outflow from I16293A causing a velocity red shift of  $0.3 \text{ km s}^{-1}$ . However, only the non-deuterated species, which predominantly reside in the outer core region, are red-shifted with respect to their deuterated forms found mainly in the heart of the core. This is exactly the velocity shift which Hirano et al. (2001) would expect from an interaction of the northeast red lobe. However, they did not detect this, since they measured only the  $\text{H}^{13}\text{CO}^+$  1–0 line at the position of I16293E which has a velocity equal to the cloud systemic velocity. Under our hypothesis this has to be measured with respect to the reference frame of the first shock.

This second shock boosted the gas-phase deuterium chemistry to its maximum and the temperature is further lowered due to further compression. We think that it is this firecracker effect which leads to the extreme deuteration of LDN 1689N in general, and I16293E in particular. Multiple shocks may be common in low-mass YSOs; Larsson et al. (2002) suggest that Serpens SMM1 is influenced by multiple low-velocity shocks driven by the outflow.

## 7. Discussion and Conclusions

We have analyzed our submillimeter dust and continuum data in terms of an excitation analysis using a model for the temperature and density structure of the disk, envelope, and outflow of I16293A, B, and E. The spectral lines of  $\text{H}_2\text{O}$ , HDO, and  $\text{H}_2\text{D}^+$  were subsequently compared with predictions from a simple chemical network.

Figure 17 shows a schematic overview of the IRAS 16293-2422 region showing its distinct physical regions (disk, warm dense core, warm envelope, cold envelope, outflow regions, etc.). For each region we indicate the derived physical parameters, and their molecular abundances. For the submillimeter disk of I16293A we derive a dust temperature  $T_d = 40 \text{ K}$ , a source size of about 800 AU, a total mass of  $1.8 \text{ M}_\odot$  and a luminosity of  $16.5 \text{ L}_\odot$  which corresponds to a gas density  $n(\text{H}_2) \geq 10^9 \text{ cm}^{-3}$ . The envelope of I16293A can be well described by a collapsing

envelope model with parameters age  $t = (0.6\text{--}2.5) \times 10^4$  yr and sound speed  $a = 0.7$  km s $^{-1}$ . In fact the center of the expansion wave,  $r_{\text{CEW}} = at$ , is 890–3700 AU from the centre which corresponds to 6–23'' at the distance of 160 pc, comparable to the beam size of the SCUBA continuum and submillimeter line emission of the species we used in the analysis. The outer radius of the envelope is about 7300 AU and the temperature ranges from 115 K in the inner region to 12 K in the outer region. The envelope mass is  $M_{\text{env}}(\text{H}_2) = 6.1$  M $_{\odot}$ . We find that for a YSO such as I16293A the line emission is better suited than the continuum emission to constrain the infall parameters. The excitation analysis of the envelope yields a constant HDO abundance of  $3 \times 10^{-10}$  throughout the envelope, and an ortho-H $_{2\text{O}}$  abundance of  $2 \times 10^{-7}$  for the regions with  $T_{\text{kin}} > 14$  K, while the abundance is lowered by a factor of 150 in the colder regions. From the C $^{17}\text{O}$  analysis we find that CO is depleted by a factor of 50 for the envelope regions where  $T_{\text{kin}} < 20$  K. The line wings of the CO, HDO, and H $_{2\text{O}}$  emission can qualitatively be explained by a single outflow model with a turbulent velocity of 2.3 km s $^{-1}$  and where the maximum outflow velocity is about 6 km s $^{-1}$ . The excitation analysis of the outflow model indicates that the ortho-H $_{2\text{O}}$  abundance in the outflow is about  $1 \times 10^{-8}$  and that the HDO abundance in the outflow is in the range of  $3 \times 10^{-9}$  to  $3 \times 10^{-10}$ . A more quantitative comparison requires a multiple outflow model. We find that only two outflows are present, a NE–SW outflow with a dynamical time scale of about  $(3.0\text{--}3.5) \times 10^3$  yr which is powered by I16293A a Class 0 source, and an E–W outflow which is a fossil flow with a dynamical time scale of  $(6.4\text{--}7.6) \times 10^3$  yr driven by I16293B which looks like a young low-luminosity T Tauri star. The prestellar object I16293E is well described with an isothermal core of  $T_{\text{kin}} = 16$  K, a core radius of 8000 AU and a power law density structure of the form  $n(r) = n_0(r/1000 \text{ AU})^{-p}$  where  $n_0 = n(R = 1000 \text{ AU}) = 1.6 \times 10^6 \text{ cm}^{-3}$ . The total mass mass of this core is  $M_{\text{core}}(\text{H}_2) = 4.35$  M $_{\odot}$ . Our excitation analysis of the core indicate a depletion of CO and HCO $^{+}$  by a factor of ten relative to the ‘standard abundances’ and that the DCO $^{+}$  abundance is larger than that of H $^{13}\text{CO}^{+}$ . Our tentative detection of HDO indicates the presence of a cold condensation in the heart of this core where the HDO abundance is about  $2 \times 10^{-10}$ . Our detailed CO mapping shows that I16293E has no outflow, so its evolutionary stage is younger than Class 0. We argue that this core may hide a first hydrostatic core, a so called Class –I object which is deeply embedded in a largely unaffected cold core.

The reason for the extreme deuteration in the L16293N cloud and in particular in I16293A, and I16293E may lie in the fact that I16293AB is a binary system where the YSOs and the outflows differ in age causing a firecracker effect of the deuteration. In this scenario the older E–W ouflow from I16293B is responsible for the formation of I16293E out of a dense dark core through a slow shock where only deuterated species were desorbed from the grains which, in combination with the low temperatures, amplifies the deuterium enrichment

in the gas phase before a possible re-absorption on grains. This strong deuterated core may have been shocked again an a later time by the younger NW–SW outflow from I16293A further boosting the gas-phase deuterium chemistry to extreme values.

It is remarkable that the abundances of many molecules in the prestellar core I16293E and in the warm part of the envelope of I16293A are comparable. In particular, the HDO abundances are similar which indicates that the warm gas in I16293A may have gone through the same cold pre-collapse phase that I16293E is currently in. A simple chemical gas-phase modeling of the deuterium chemistry requires that CO is depleted by a facor of 50 for  $T_{\text{kin}} < 22$  K in order to reproduce the observed  $\text{H}_2\text{D}^+$  emission from our chemical network applied to the envelope ( $T, n$ ) structure, and that an  $\text{H}_2\text{O}$  abundance of  $3 \times 10^{-7}$  for  $T_{\text{kin}} > 14$  K and  $4 \times 10^{-9}$  for  $T_{\text{kin}} < 14$  K is required to reproduce the observed spectrum from the chemical model. The  $[\text{HDO}]/[\text{H}_2\text{O}]$  abundance in the warm inner-envelope of I16293A ( $2 \times 10^{-4}$ ) is close to the value that has been measured in the solar system and supports this. Our chemical modeling indicates that the  $[\text{HDO}]/[\text{H}_2\text{O}]$  ratio is determined in the cold gas phase prior to star formation, and that this ratio is conserved in the early stages of low-mass star through freeze out on dust grains formation and that the molecules are released unprocessed to the gas phase after the formation of a low-mass YSO. If this warm deuterated gas is subsequently locked-up in a proto-planetary disk before the high temperature gas chemistry causes a de-deuteration, the  $[\text{D}]/[\text{H}]$  ratio of HDO in low-mass pre-solar systems would remain conserved. To investigate this scenario in detail, sensitive follow-up observations of the HDO and  $\text{H}_2\text{O}$  ground-state transitions in a large sample of low-mass YSOs are needed at high spatial and spectral resolution (i.e., interferometry from high altitudes  $[\text{HDO}]$  and from space  $[\text{H}_2\text{O}]$ ) and allow a study of the  $[\text{HDO}]/[\text{H}_2\text{O}]$  abundance evolution from prestellar cores to planets. The  $\text{H}_2^{18}\text{O}$  ground-state transition may be more suitable than the ortho- $\text{H}_2\text{O}$  transition since the ground-state of the latter molecule is at  $\Delta E/k = 34.3$  K above ground, while that of  $\text{H}_2^{18}\text{O}$  is at 0 K, and the main isotopic form of water is expected to be mostly optically thick in its ortho and para ground-state lines.

The James Clerk Maxwell Telescope is operated by the Joint Astronomy Centre, on behalf of the Particle Physics and Astronomy Research Council of the United Kingdom, the Netherlands Organisation for Scientific Research, and the National Research Council of Canada. It is a pleasure to thank the JCMT staff and the MPIfR Division for Submillimeter Technology for their outstanding support. The Canadian Astronomy Data Center is operated by the Dominion Astrophysical Observatory for the National Research Council of Canada's Herzberg Institute of Astrophysics.

## REFERENCES

Aikawa, Y., & Herbst E. 1999, *ApJ*, 526, 314

Aikawa, Y., Ohashi, N., Inutsuka, S-I., Herbst, E., & Takakuwa, S. 2001, *ApJ*, 552, 639

Aikawa, Y., van Zadelhoff, G.-J., van Dishoeck, E. F., & Herbst, E. 2002, *A&A*, 386, 622

André, P., Ward-Thompson, D., & Barsony, M. 1993, *ApJ*, 406, 122

Ashby, M. L. N., et al. 2000, *ApJ*, 539, L115

Bally, J., & Devine, D. 1997, in *Herbig-Haro Flows and the Birth of Stars*, IAU Symp. 182, ed. B. Reipurth & C. Bertout (Dordrecht: Kluwer), 29

Barsony, M., Ward-Thompson, D., André, P., & O'Linger, J. 1998, *ApJ*, 509, 733

Bergin, E. A., Neufeld, D. A., & Melnick, G. J. 1999, *ApJ*, 510, L145

Bergin, E. A., Alves, J., Huard, T., & Lada, C. J. 2002, *ApJ*, 570, L101

Bieging, J. H., & Cohen, M. 1985, *ApJ*, 289, L5

Blake, G. A., van Dishoeck, E. F., Jansen, D. J., Groesbeck, T. D., & Mundy, L. G. 1994, *ApJ*, 428, 680

Bockelée-Morvan, D., et al. 1998, *Icarus*, 133, 147

Bontemps, S., André, P., Terebey, S., & Cabrit, S. 1996, *A&A*, 311, 858

Boss, A. P., Yorke, H. W. 1995, *ApJ*, 439, L55

Brown, P. D., & Millar, T. J. 1989, *MNRAS*, 237, 661

Butner, H. M., Lada, E. A., & Loren, R.B. 1995, *ApJ*, 448, 207

Caselli, P., Walmsley, C. M., Zucconi, A., Tafalla, M., Dore, L., & Myers, P. C. 2002, *ApJ*, 565, 344

Caselli, P., van der Tak, F. F. S., Ceccarelli, C., & Bacmann, A. 2003, *A&A*, 403, L37

Castets, A., Ceccarelli, C., Loinard, L., Caux, E., & Lefloch, B. 2001, *A&A*, 375, 40

Ceccarelli, C., Hollenbach, D. J., & Tielens, A. G. G. M. 1996, *ApJ*, 471, 400

Ceccarelli, C., Castets, A., Loinard, L., Caux, E., & Tielens, A. G. G. M. 2000, A&A, 331, 372

Choi, M., Panis, J.-F., & Evans II, N. J. 1999, ApJS, 122, 519

Doty, S. D., & Neufeld, D. A. 1997, ApJ, 489, 122

Duncan, W. D., Robson, E. I., Ade, P. A. R., Griffin, M. J., & Sandell, G. 1990, MNRAS, 243, 126

Eberhardt, P., Reber, M., Krankowsky, D., & Hodges, R. R. 1995, A&A, 302, 301

Eislöffel, J., & Mundt, R. 1997, AJ, 114, 280

Emerson, D. T., Klein, U., & Haslam, C. G. T. 1979, A&A, 76, 92

Estalella, R., Anglada, G., Rodríguez, L. F., & Garay, G. 1991, ApJ, 371, 626

Garay, G., Mardones, D., Rodríguez, L.F., Caselli, P., & Bourke, T. L. 2002, ApJ, 567, 980

Gensheimer, P. D., Mauersberger, R., & Wilson, T. L. 1996, A&A, 314, 281

Green, S. 1989, ApJS, 70, 813

Guélin, M., Langer, W., & Wilson, R. W. 1982, A&A, 107, 107

Haslam, C. G. T. 1974, A&AS, 15, 333

Helmich, F. P., et al. 1996a, A&A, 315, L173

Helmich, F. P., van Dishoeck, E. F., & Jansen, D. J. 1996b, A&A, 313, 657

Herbst, E. 1982, ApJ, 252, 810

Hildebrand, R. H. 1983, QJRAS, 24, 267

Hirano, N., Mikami, H., Umemoto, T., Yamamoto, S., Taniguchi, Y. 2001, ApJ, 547, 899

Hogerheijde, M. R. & Sandell, G. 2000, ApJ, 534, 880

Hogerheijde, M. R. & van der Tak, F. F. S. 2000, A&A, 362, 697

Holland, W. S., Gear, W. K., Lightfoot, J. F., Jenness, T., Robson, E. I., Cunningham, & C. R., Laidlaw, K. 1998, in Proc. SPIE Vol. 3357, Advanced Technology MMW, Radio, and Terahertz Telescopes, ed. T. G. Phillips (Bellingham: SPIE Press), 305

Jacq, T., Walmsley, C. M., Henkel, C., Baudry, A., Mauersberger, R., & Jewell, P. R. 1990, *A&A*, 228, 447

Jenness, T. & Lightfoot, J. F. 1998, in *ASP Conf. Ser. 145, Astronomical Data Analysis Software and Systemes VII*, ed. R. Albrecht et al. (San Francisco: ASP), 216

Jensen, M. J., Bilodeau, R. C., Safvan, C. P., Seiersen, K., Andersen, L. H., Pedersen, H. B., & Heber, O. 2000, *ApJ*, 534, 764

Knee, L. B. G. & Sandell, G. 2000, *A&A*, 361, 671

Lada, C. J., 1991, in *NATO-ASI Ser. 342, The Physics of Star Formation and Early Stellar Evolution*, ed. C. J. Lada & N. D. Kylafis (Dordrecht: Kluwer), 329

Larsson, B., Liseau, R., & Men'shchikov, A. B. 2002, *A&A*, 386, 1055

Lécuyer, C., Gillet, Ph., & Robert, F. 1998, *Chemical Geology*, 145, 249

Lepp, S., Dalgarno, A., & Sternberg, A. 1987, *ApJ*, 321, 383

Lis, D. C., Gérin, M., Phillips, T. G., & Motte, F. 2002, *ApJ*, 569, 322

Liseau, R., & Sandell, G. 1986, *ApJ*, 304, 459

Looney, L. W., Mundy, L. G., & Welch, W. J. 2000, *ApJ*, 529, 477

Meier, R., Owen, T. C., Matthews, H. E., Jewitt, D. C., Bockelée-Morvan, D., Biver, N., Crovisier, J., & Gauthier, A. 1998, *Science*, 279, 842

Melnick, G. J., Stauffer, J. R., Ashby, M. L. N., Bergin, E. A., Chin, G. 2000, *ApJ*, 539, L77

Mezger, P. G., Sievers, A., Zylka, R., Haslam, C. G. T., Kreysa, E., & Lemke, R. 1992, *A&A*, 265, 743

Millar, T. J., Bennett, A., & Herbst, E. 1989, *ApJ*, 340, 906

Millar, T. J., Herbst, E., & Charnley, S. B. 1991, *ApJ*, 369, 147

Mizuno, A., Fukui, Y., Nozawa, S., & Takano, T. 1990, *ApJ*, 356, 184

Motte, F., André, P., & Neri, R. 1998, *A&A*, 336, 150

Mundy, L. G., Wilking, B. A., & Myers, S. T. 1986, *ApJ*, 311, L75

Mundy, L. G., Wootten, A., & Wilking, B. A. 1990, *ApJ*, 352, 159

Mundy, L. G., Wootten, A., Wilking, B. A., Blake, G. A., & Sargent, A. I. 1992, *ApJ*, 385, 306

Narayanan, G., Walker, C. K., & Buckley, H. D. 1998, *ApJ*, 496, 292

Neufeld, D. A., Ashby M. L. N., Bergin, E. A., Chin, G., Erickson, N. R. 2000, *ApJ*, 539, L107

Olberg, M., Bester, M., Rau, G., et al. 1985, *A&A*, 142, L1

Ossenkopf, V. & Henning, Th. 1994, *A&A*, 291, 943

Padman, R., Bence, S., & Richer, J. 1997, in *Herbig-Haro Flows and the Birth of Stars*, IAU Symp. 182, ed. B. Reipurth & C. Bertout (Dordrecht: Kluwer), 123

Phillips, T. G., van Dishoeck, E. F., & Keene, J. 1992, *ApJ*, 399, 533

Phillips, T. R., Maluendes, S., & Green, S. 1996, *ApJS*, 107, 467

Pineau des Forêts, G., Roueff, E., & Flower, D. R. 1989, *MNRAS*, 240, 167

Richer, J. S. 1992, *MNRAS*, 254, 165

Rodgers, S. D., & Millar, T. J., 1996 *MNRAS*, 280, 1046

Rodríguez, L. F., Cantó, J., Torellas, J. M., & Ho, P. T. P. 1986, *ApJ*, 301, L25

Sandell, G. 1994, *MNRAS*, 271, 75

Sandell, G., Jessop, N., and Jenness, T. 2001, The SCUBA Map Reduction Cookbook, Starlink Cookbook 11.2, <http://www.starlink.rl.ac.uk/star/docs/sc11.htm#xref>

Sault, R. J., Teuben, P. J., & Wright, M. C. H., 1995, in *ASP Conf. Ser.* 77, *Astronomical Data Analysis Software and Systemes IV*, ed. R. A. Shaw et al. (San Francisco: ASP), 433

Schöier, F. L., Jørgensen, J. K., van Dishoeck, E. F., & Blake, G. A. 2002, *A&A*, 390, 1001

Schöier, F. L., Jørgensen, J. K., van Dishoeck, E. F., & Blake, G. A. 2003, in *Chemistry as a Diagnostic of Star Formation*, ed. C. L. Curry & M. Fich (Ottawa: NRC Press), in press

Shah, R. Y. & Wootten A. 2001, *ApJ*, 554, 933

Shirley, Y. L., Evans, N. J., II, Rawlings, J. M. C., & Gregersen, E. M. 2002, *ApJS*, 131, 249

Shu, F. H. 1977, *ApJ*, 214, 488

Schulz, A., Güsten, R., Walmsley, C. M., & Serabyn, E. 1991, *A&A*, 246, L55

Smith, D., Adams, N.G., & Alge, E. 1982, *ApJ*, 263, 123

Snell, R. L., Howe, J. E., Ashby, M. L. N., Bergin, E. A., Chin, G., et al. 2000, *ApJ*, 539, L101

Stark, R., van der Tak, F. S. S., & van Dishoeck, E. F. 1999, *ApJ*, 521, L67

Tielens, A. G. G. M. 1989, in *Proc. IAU Symp. 135, Interstellar Dust*, ed. L. J. Allamandola & A. G. G. M. Tielens (Dordrecht: Kluwer), 239

van Dishoeck, E. F., Blake, G. A., Jansen, D. J., & Groesbeck, T. D. 1995, *ApJ*, 447, 760

Walker, C. K., Lada, C. J., Young, E. T., Maloney, P. R., & Wilking, B. A. 1986, *ApJ*, 309, L47

Walker, C. K., Lada, C. J., Young, E. T., & Margulis, M. 1998, *ApJ*, 332, 335

Walker, C. K., Carlstrom, J. E., & Bieging, J. H. 1993, *ApJ*, 402, 655

Watson, W. D., Anichich, V. G., & Huntress, W. T., Jr. 1976, *ApJ*, 205, L165

Williams, J. P., Bergin, E. A., Caselli, P., Myers, P. C., & Plume, R. 1998, *ApJ*, 503, 689

Wilson, T. L. & Rood, R. 1994, *ARA&A*, 32, 191

Wolf-Chase, G. A., Barsony, M., & O'Linger, J. 2000, *ApJ*, 120, 1467

Wootten, A., & Loren, R. B. 1987, *ApJ*, 317, 220

Wootten, A. 1987, in *Proc. IAU Symp. 120, Astrochemistry*, ed. M. S. Vardya & S. P. Tarafdar (Dordrecht: Kluwer), 311

Wootten, A. 1989, *ApJ*, 337, 858

Table 1. Submillimeter Photometry of I16293E and Total Flux Densities of I16293A, B  
Derived From Maps

Filter/HPBW	I16293E	I16293AB	
	Flux Density (Jy beam <sup>-1</sup> )	Integrated Flux (Jy beam <sup>-1</sup> )	Envelope (Jy)
2.0 mm/27'' (2)	0.20 ± 0.03		
1.3 mm/19.5'' (1)	0.60 ± 0.05	7.0 ± 1.4 <sup>a</sup>	
1.1 mm/18.5'' (3)	0.70 ± 0.07	8.6 ± 0.9	
850 $\mu$ m/14.5''	...	21.9 ± 2.2	16.0
850 $\mu$ m/14.0''	1.40 ± 0.02 <sup>b</sup>	20.4 ± 0.03 <sup>c</sup>	
800 $\mu$ m/16.5'' (2)	2.06 ± 0.11	24.5 ± 2.5	
750 $\mu$ m/13.3''	...	26.6 ± 10.0	
450 $\mu$ m/18'' (2)	11.8 ± 2.2	126 ± 15	102.7
450 $\mu$ m/8.0''	4.35 ± 0.09 <sup>b</sup>	126 ± 0.2 <sup>c</sup>	
350 $\mu$ m/19'' (1)	19.4 ± 2.3	175 ± 35	

Note. — Numbers in parentheses denote the number of independent observations obtained for each filter/aperture combination.

<sup>a</sup>from Mezger et al. (1992).

<sup>b</sup>Peak flux density in cleaned SCUBA maps, see text.

<sup>c</sup>Integrated flux from Gaussian fit to SCUBA map. Errors are  $1\sigma$  and do not account for systematic calibration uncertainties.

Table 2. Molecular Line Observations of I16293AB and I16293E

Molecule	Transition	$\int T dV$ (K km s <sup>-1</sup> )	T (K)	$\Delta V$ (km s <sup>-1</sup> )	$V_{\text{LSR}}$ (km s <sup>-1</sup> )
I16293A B, in units of $T_{\text{MB}}$					
C <sup>18</sup> O	3-2	33.3			4.0
	2-1	18.4	6.50	2.50	3.76
C <sup>17</sup> O	2-1	9.3	3.24	2.86	3.99
<sup>12</sup> CO	7-6	473			3.9
	6-5	408			3.9
HCO <sup>+</sup>	4-3	81			4.1
	3-2	70			4.0
H <sup>13</sup> CO <sup>+</sup>	4-3	7.2			4.7
H <sup>13</sup> CO <sup>+</sup>	3-2 <sup>a</sup>	11.8	4.87	2.27	4.23
	3-2 <sup>b</sup>	-2.3	-2.76	0.78	4.24
DCO <sup>+</sup>	5-4	3.1			4.0
	3-2	5.18	2.56	2.02	4.48
H <sub>2</sub> D <sup>+</sup>	1 <sub>10</sub> -1 <sub>11</sub>	0.8	1.1	0.6	3.9
N <sub>2</sub> H <sup>+</sup>	4-3	4.4	2.6	1.7	3.7
HDO	1 <sub>01</sub> -0 <sub>00</sub> <sup>a</sup>	6.0	1.0	5.9	4.3
	1 <sub>01</sub> -0 <sub>00</sub> <sup>b</sup>	-1.4	-2.1	0.60	4.2
H <sub>2</sub> O	1 <sub>10</sub> -1 <sub>01</sub>	2.9			3.9
I16293E, in units of $T_R^*$					
C <sup>18</sup> O	2-1	5.40	3.60	1.41	3.80
C <sup>17</sup> O	2-1	1.70	1.26	1.27	4.03
H <sup>13</sup> CO <sup>+</sup>	3-2	1.64	1.25	1.23	4.08
DCO <sup>+</sup>	3-2	3.74	3.14	1.12	3.76
HDO	1 <sub>10</sub> -1 <sub>11</sub>	0.1	0.15	0.6	3.5

Note. — For those spectra where we only list the integrated intensity,  $V_{\text{LSR}}$  is the velocity of the self-absorption.

<sup>a</sup>Emission component.

<sup>b</sup>Absorption component.

Table 3. Turbulent Line Width  $b$  and Inferred Abundances for I16293AB and I16293E

Species	I16293A, B		Envelope Abundance	Envelope Abundance <sup>a</sup>	Outflow Abundance
	I16293E Abundance	$b$ (km s <sup>-1</sup> )			
C <sup>18</sup> O	3(-8)	0.83	2(-7)	6.2(-8)	
C <sup>17</sup> O	9(-9)	0.76	4(-8)	1.6(-8)	
HCO <sup>+</sup>	1(-10)	0.69	< 1(-9)	1.4(-9)	
H <sup>13</sup> CO <sup>+</sup>	2(-11)	0.50	2(-11)	2.4(-11)	
DCO <sup>+</sup>	5(-11)	0.67	2(-11)	1.3(-11)	
H <sub>2</sub> O			3(-7) <sup>b</sup> 4(-9) <sup>c</sup>		1.3(-8)
HDO	2(-10)	0.20	3(-10)		
H <sub>2</sub> D <sup>+</sup>			1(-12) <sup>d</sup> 2(-9) <sup>e</sup>		
N <sub>2</sub> H <sup>+</sup>			3(-11)		
H <sub>3</sub> O <sup>+</sup>			< 5(-9)		

Note. —  $c(-d)$  denotes  $c \times 10^{-d}$ .

<sup>a</sup>Abundance derived by Schöier et al. (2002) in a similar analysis.

<sup>b</sup>Where  $T_{\text{kin}} > 14$  K.

<sup>c</sup>Where  $T_{\text{kin}} < 14$  K.

<sup>d</sup>Where  $T_{\text{kin}} > 20$  K.

<sup>e</sup>Where  $T_{\text{kin}} < 20$  K.

Table 4. Physical Parameters of the NE–SW Outflow

Parameter	Uncorrected <sup>a</sup>		Corrected <sup>b</sup>	
	SW Blue	NE Red	SW Blue	NE Red
Dynamical time scale (yr)	$6.4 \times 10^3$	$7.6 \times 10^3$	$3.0 \times 10^3$	$3.5 \times 10^3$
Mass ( $M_\odot$ )	0.10	0.05	0.33	0.18
Momentum ( $M_\odot \text{ km s}^{-1}$ )	0.60	0.22	2.27	1.25
Energy ( $M_\odot \text{ km}^2 \text{ s}^{-2}$ )	3.44	0.78	23.4	8.64
Force ( $10^{-5} M_\odot \text{ km s}^{-1} \text{ yr}^{-1}$ )	1.91	0.74	6.43	4.90

<sup>a</sup>Uncorrected for opacity and inclination.

<sup>b</sup>Corrected for opacity and inclination.

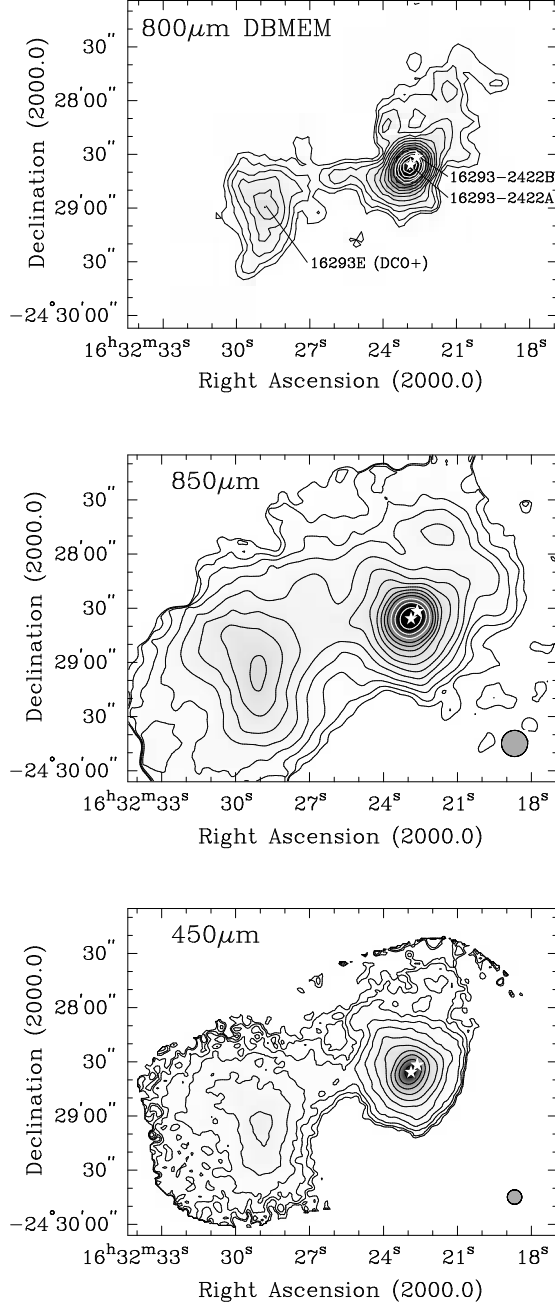


Fig. 1.— Continuum maps of IRAS 16293–2422A, B and I16293E, all shown in greyscale enhanced with logarithmic contours. *Top*: 800  $\mu\text{m}$  UKT14 map. The position of the core I16293E and the two protostars I16293A and B are indicated. The lowest contour is at 0.1 Jy pixel $^{-1}$  (3" pixels) and peak flux density is 1.8 Jy pixel $^{-1}$ . *Middle*: 850  $\mu\text{m}$  SCUBA map. The lowest countour is at 0.1 Jy beam $^{-1}$ , peak flux is 16.0 Jy beam $^{-1}$ . *Bottom*: 450  $\mu\text{m}$  SCUBA map. The lowest contour is at 1 Jy beam $^{-1}$ , peak at 76.1 Jy beam $^{-1}$ . The excess noise seen in the outskirts of the map is not real but due to edge effects. The effect from blanked negative bolometers north of I16293A, B is evident. The HPBW is indicated for the 850 and 450  $\mu\text{m}$  maps.

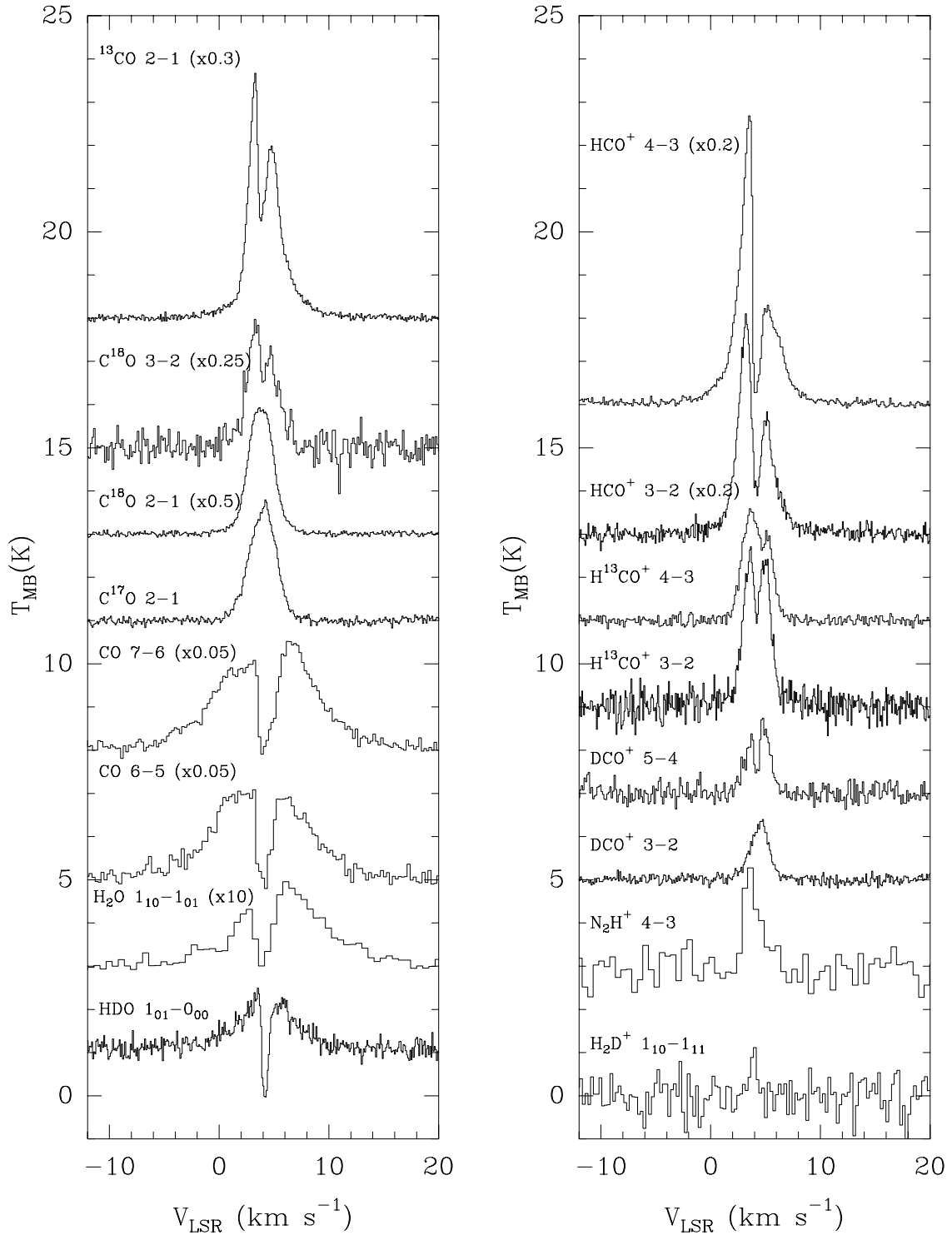


Fig. 2.— Observed spectra toward I16293A.

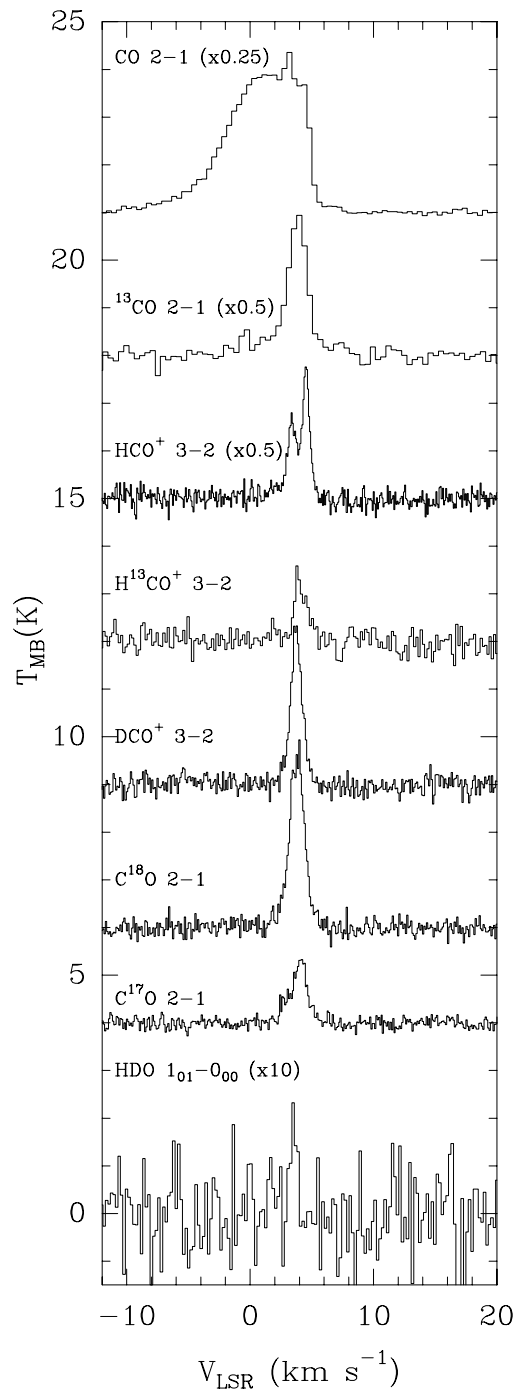


Fig. 3.— Observed spectra toward I16293E.

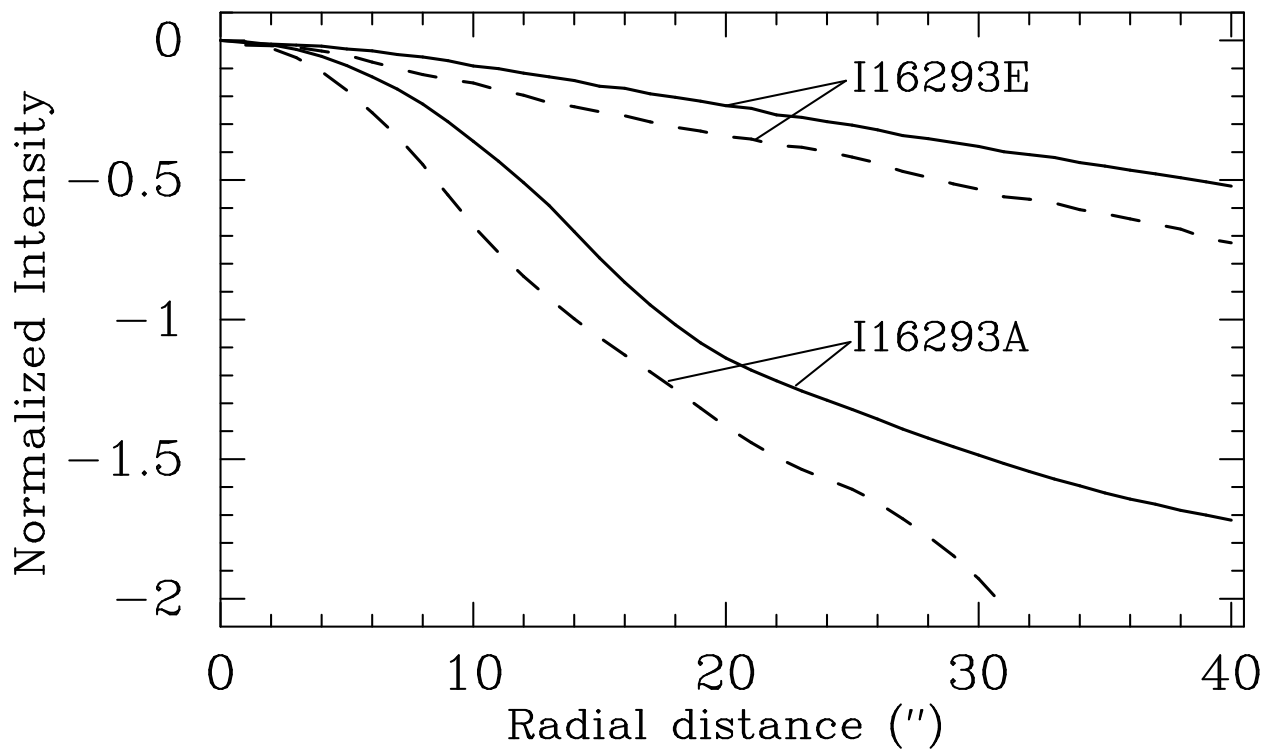


Fig. 4.— Azimuthally averaged flux densities of I16293A and I16293E at  $850\,\mu\text{m}$  (solid curves) and  $450\,\mu\text{m}$  (dashed curves).

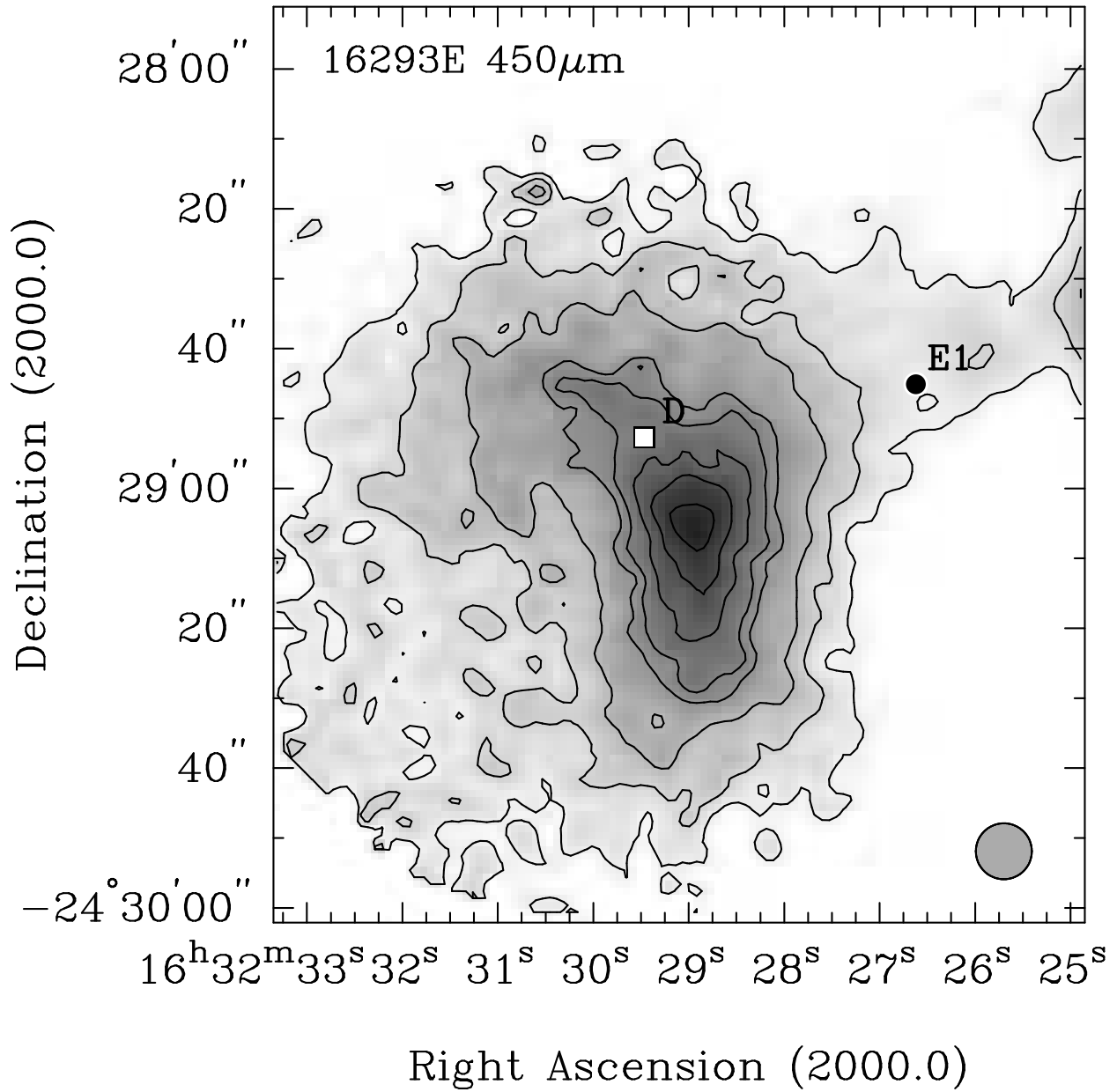


Fig. 5.— Blow-up of the 450  $\mu$ m SCUBA image of I16293E. The deuterium peak position D (white square; Lis et al. 2002) and the peak of the SiO emission E1 (black dot; Hirano et al. 2001) are indicated.

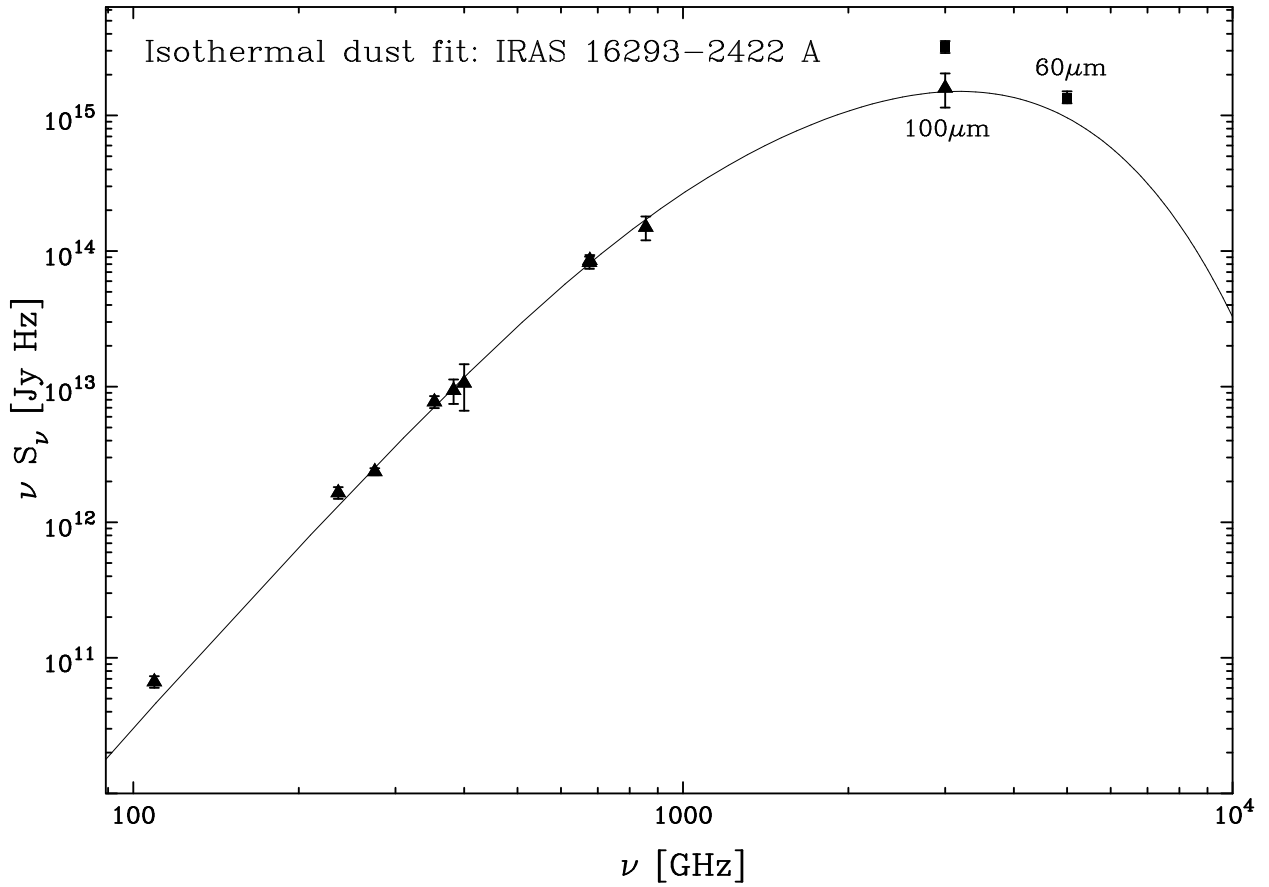


Fig. 6.— Isothermal fit to the continuum emission from I16293A. For the IRAS  $100\mu\text{m}$  data we show the total flux, as well as the flux estimated to come from the dust disk alone. The 2.75 mm (109 GHz) point from Mundy et al. (1990) is also shown. This data point also includes free-free emission from both A and B and was not used in the fit.

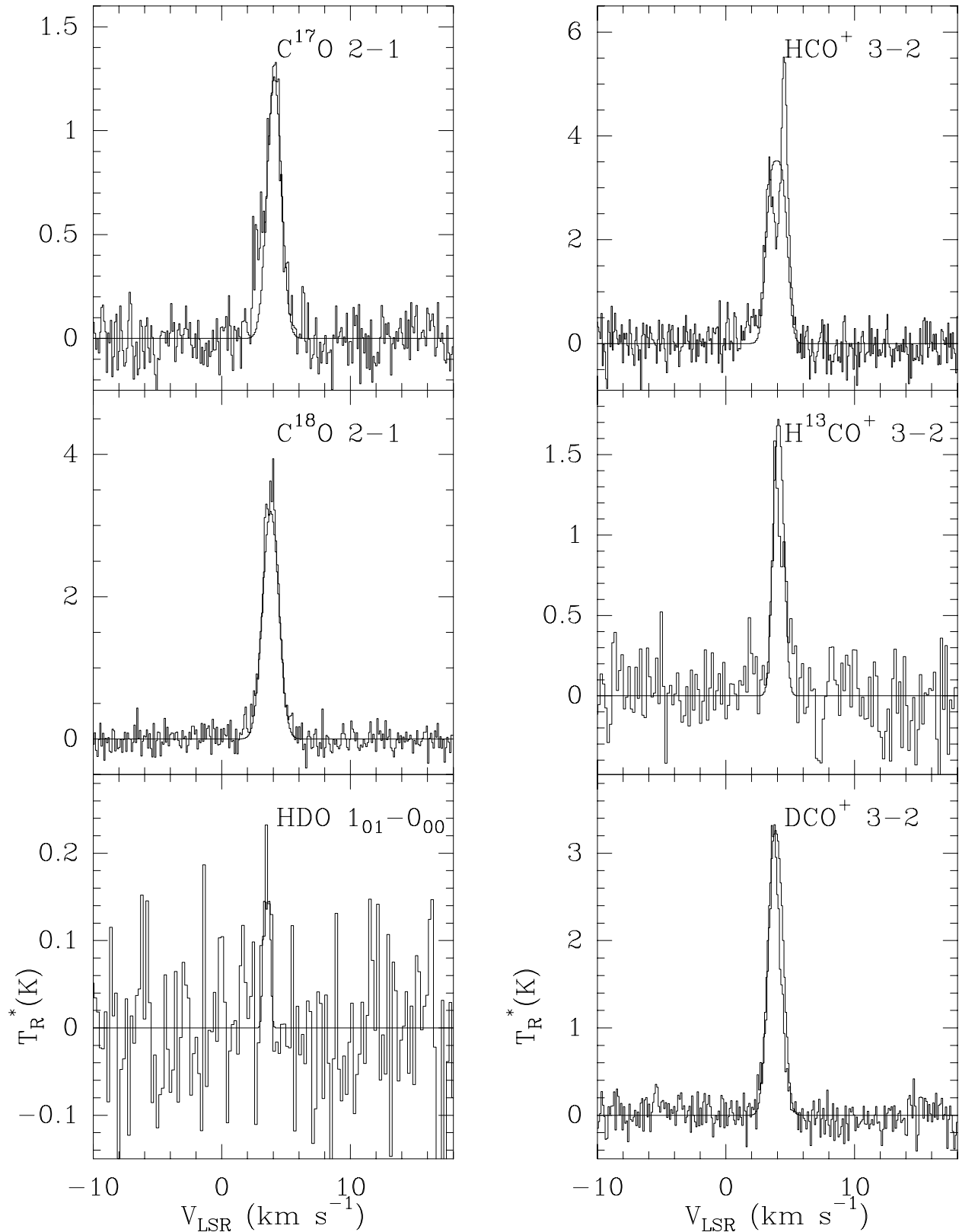


Fig. 7.— Observed spectra toward I16293E overlaid with best-fit line profiles from an isothermal core model with a power-law density distribution.

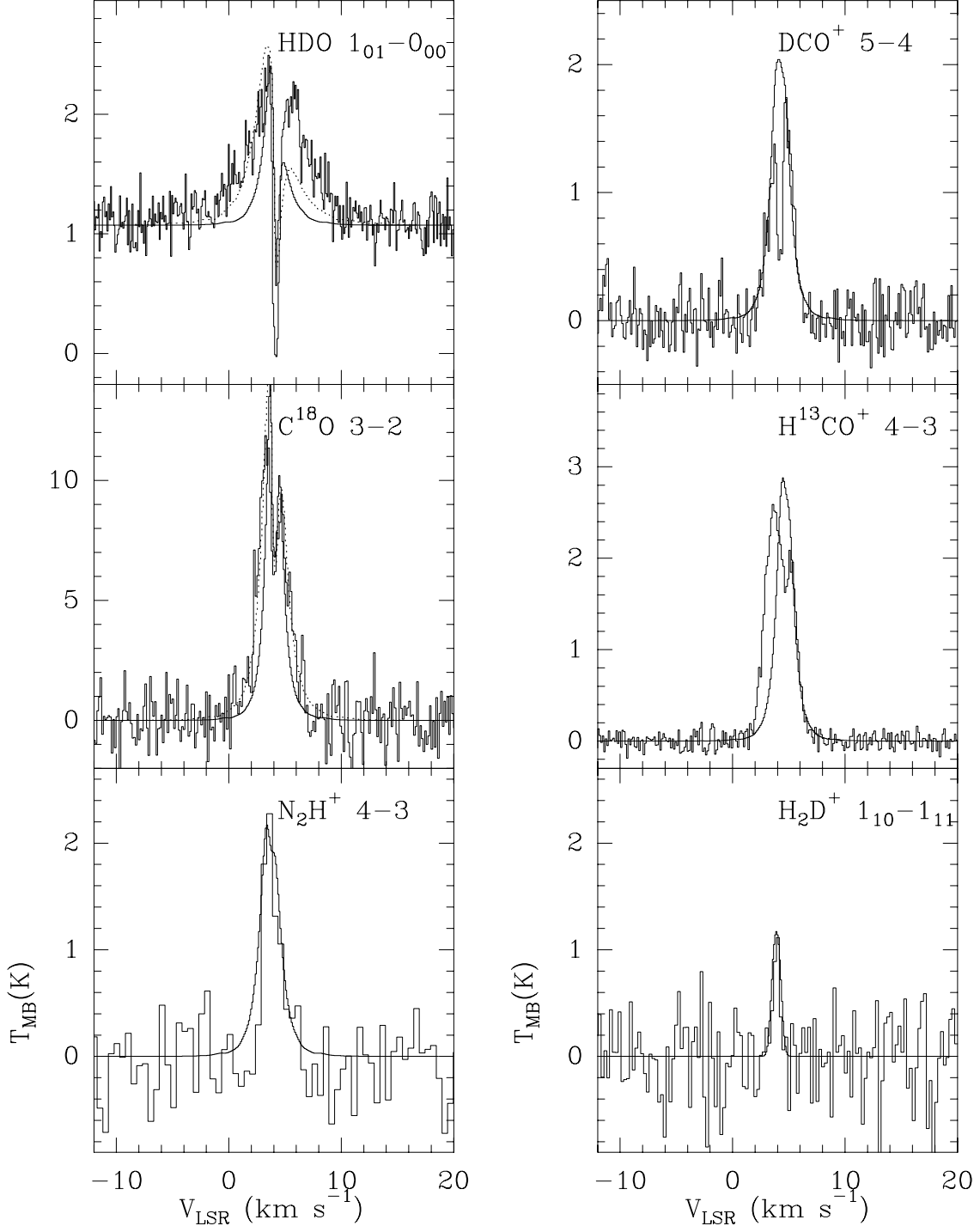


Fig. 8.— Selection of observed spectra toward I16293A overlaid with line profiles predicted by the inside-out collapse model for a sound speed  $a=0.7 \text{ km s}^{-1}$  and age  $t=2.5 \times 10^4 \text{ yr}$ . A better fit to the wings of the  $\text{C}^{18}\text{O}$  and HDO spectra is obtained for a sound speed  $a = 0.9 \text{ km s}^{-1}$  and  $a = 1 \text{ km s}^{-1}$ , respectively (dotted curves).

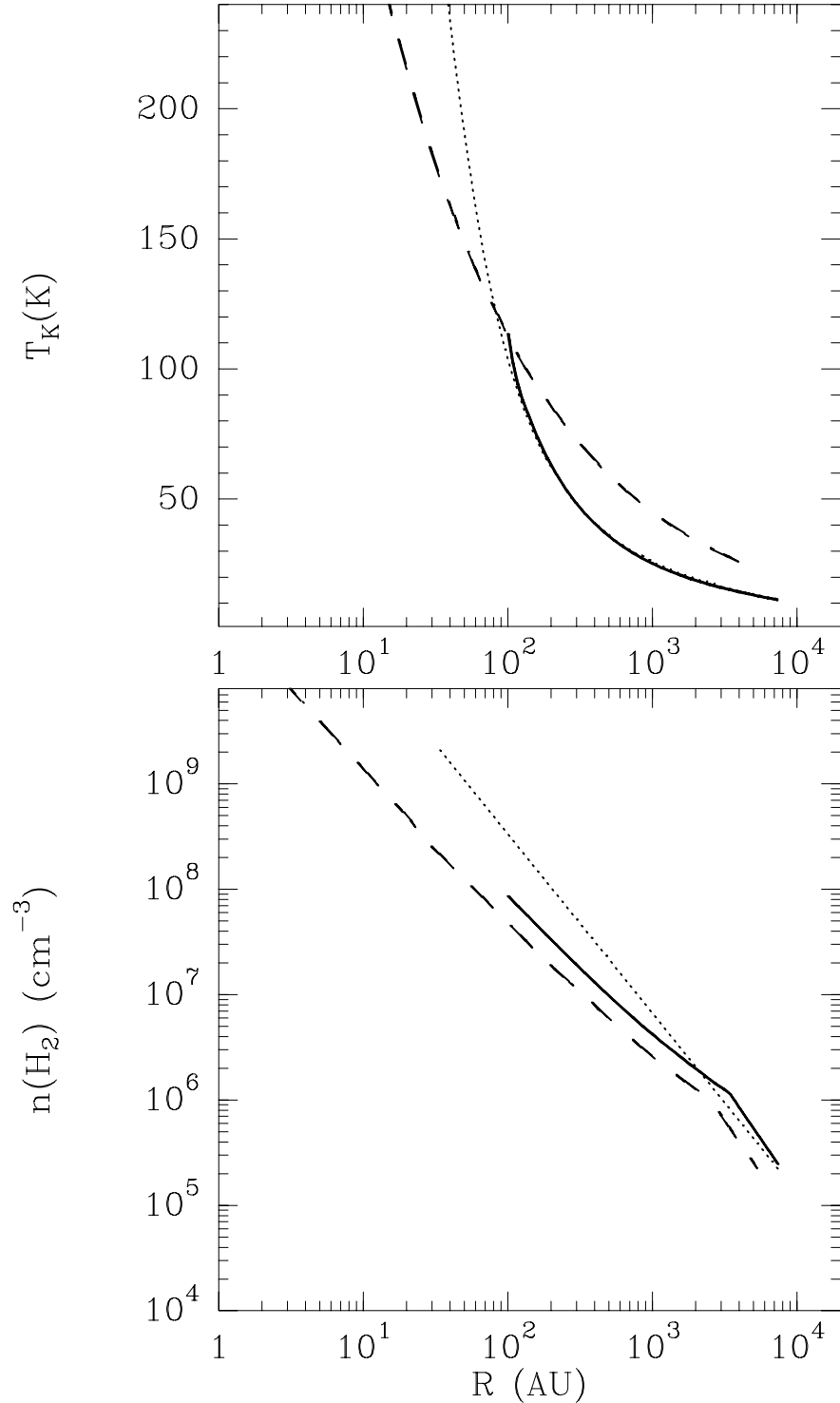


Fig. 9.— Comparison of our power-law density and temperature distributions (*solid curves*) with those of Schöier et al. (2002) (*dotted*) and Ceccarelli et al. (2000) (*dashed curves*).

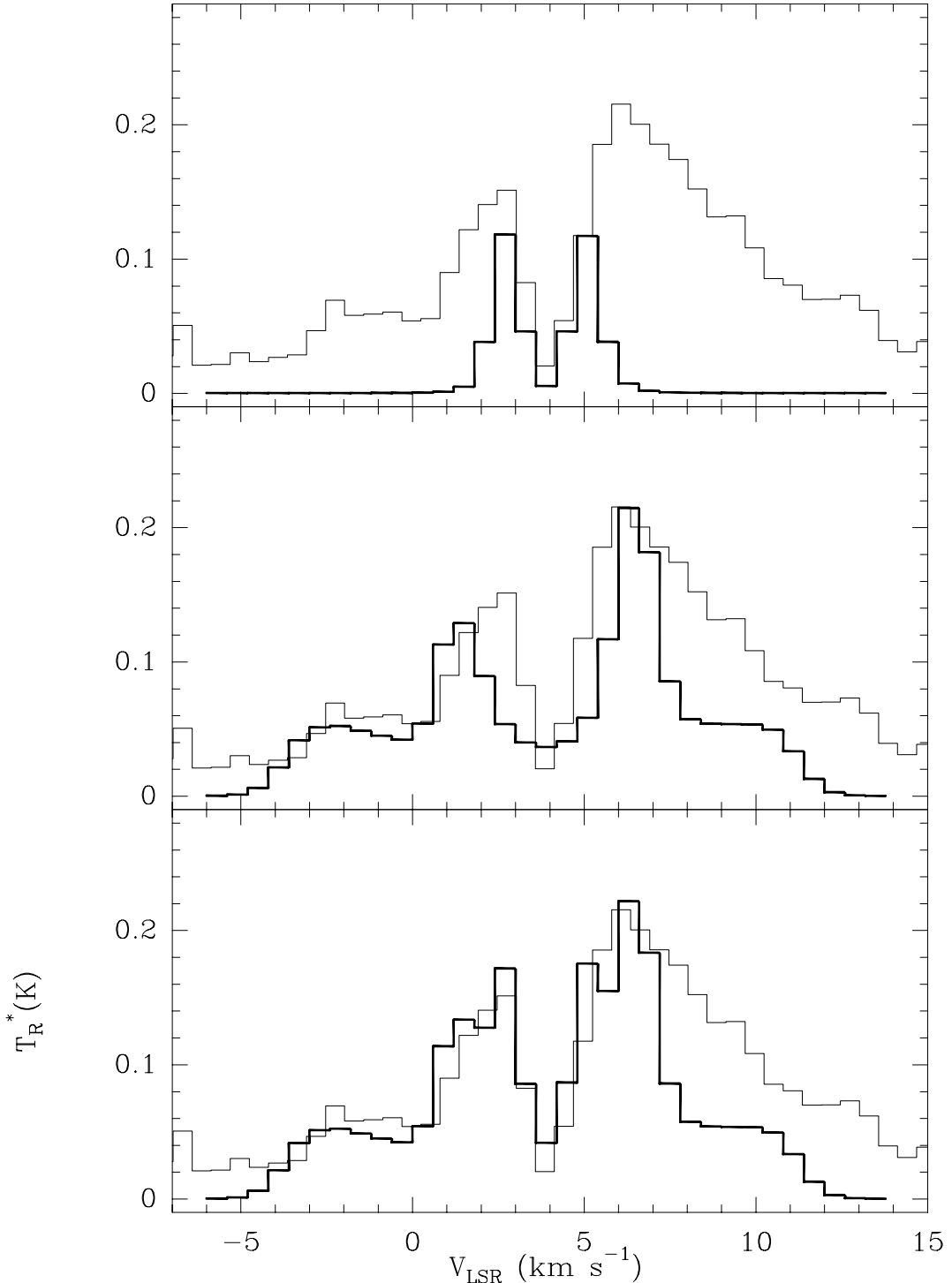


Fig. 10.— Observed H<sub>2</sub>O spectrum (*thin curves*) from SWAS overlayed with our collapse envelope model spectrum (*top panel*); the outflow model spectrum (*middle*); and the coadded infall and outflow spectra (*bottom*).

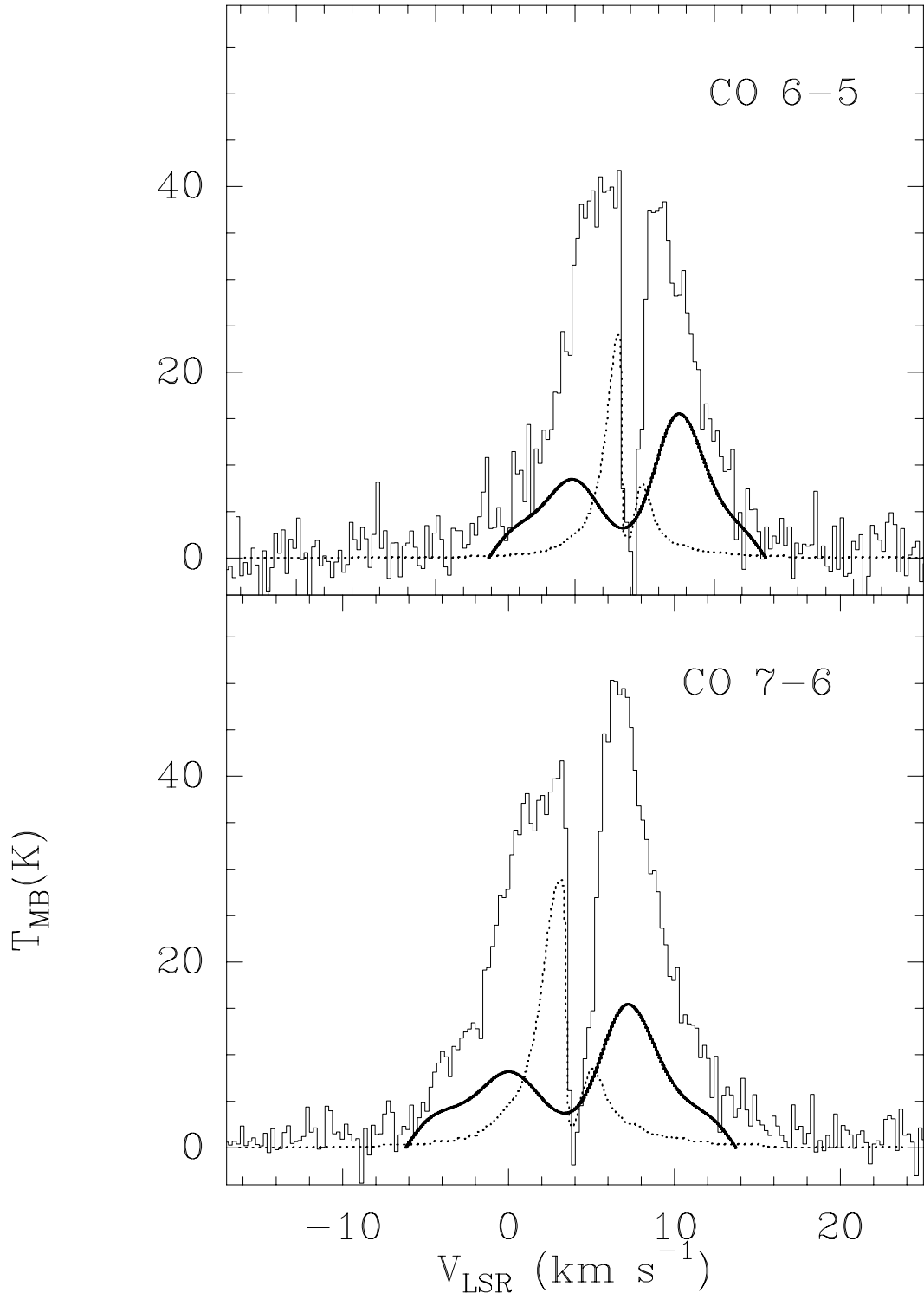


Fig. 11.— Observed CO  $J=6-5$  and  $7-6$  spectra toward I16293A together with overlaid infall (dotted) and outflow (thick) model profiles for a  $[\text{CO}]/[\text{H}_2]$  abundance of  $10^{-4}$ .

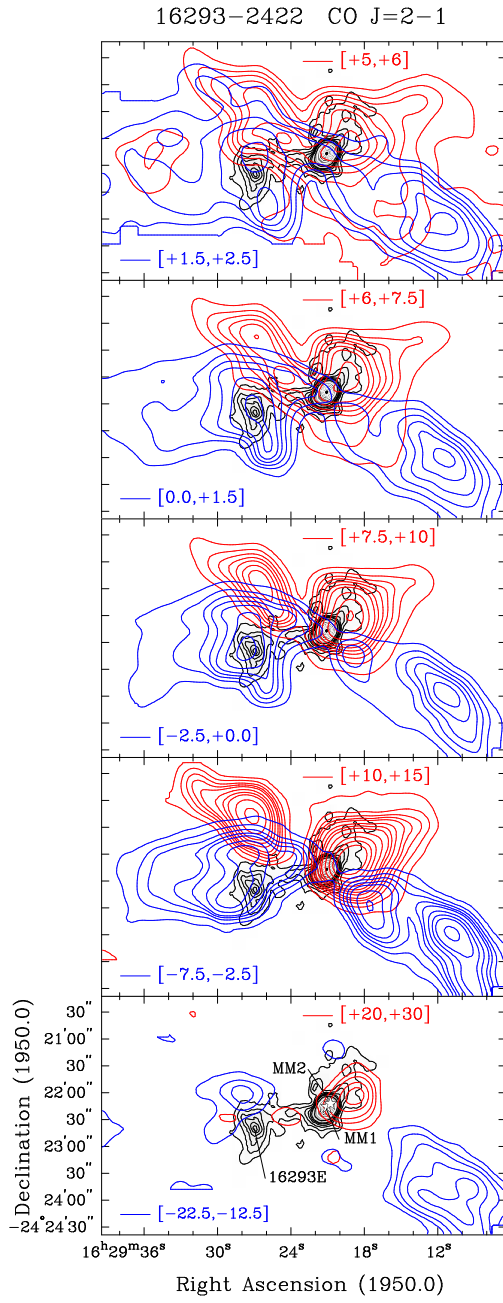


Fig. 12.— Contour plots of the two outflows from IRAS 16293–2422 A and B for indicated velocity intervals superposed on our 800  $\mu$ m continuum image.

Fig. 13.— Velocity position contour plots of the two outflows driven by IRAS 16293–2422 A and B. The top figure is created by rotating the map with the position angle of the outflow  $-35^\circ$  and integrating over a  $20''$  wide strip approximately centered on A, i.e. this velocity position diagram goes along the symmetry axis of the NE–SW outflow, but also includes some contribution from the E–W outflow driven by B. The bottom plot is derived by rotating the CO map by  $96^\circ$  and integrating over a  $20''$  wide strip approximately centered on B.

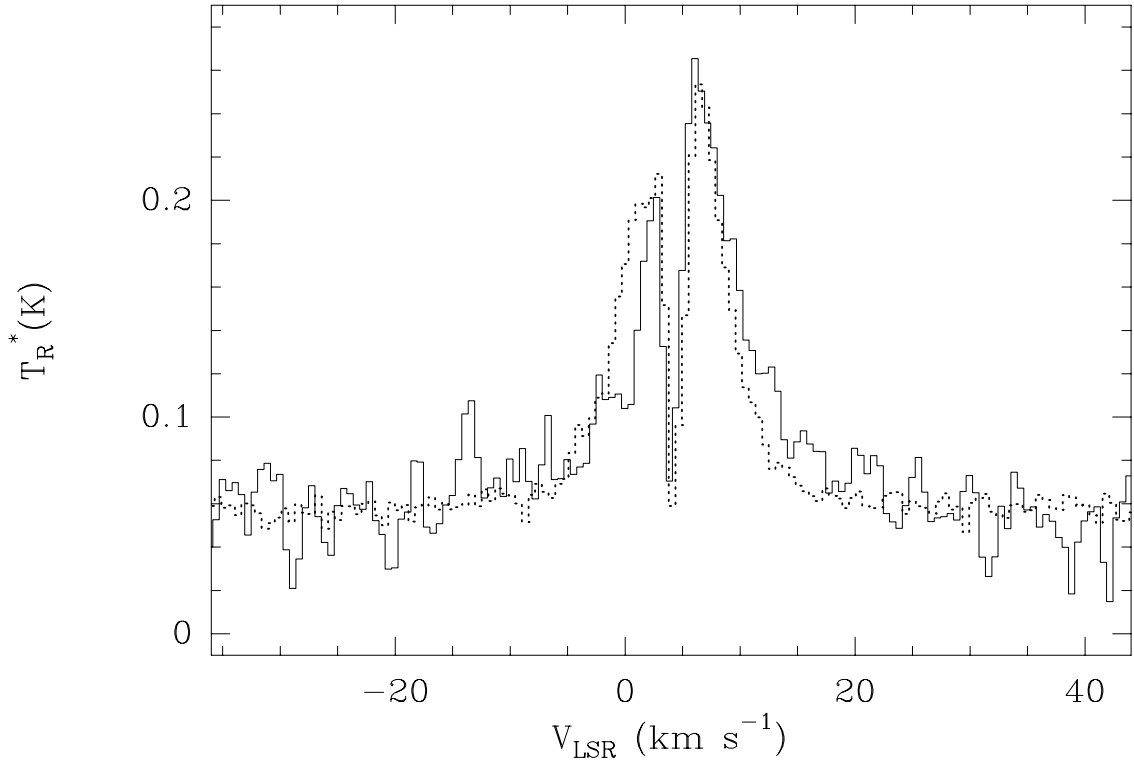


Fig. 14.—  $\text{H}_2\text{O}$  spectrum from SWAS (thick line) superposed on the CO  $J=7-6$  emission measured with the JCMT (dotted line). The CO emission has smoothed to the same spectral resolution as SWAS and scaled down to match the peak of the  $\text{H}_2\text{O}$  emission.

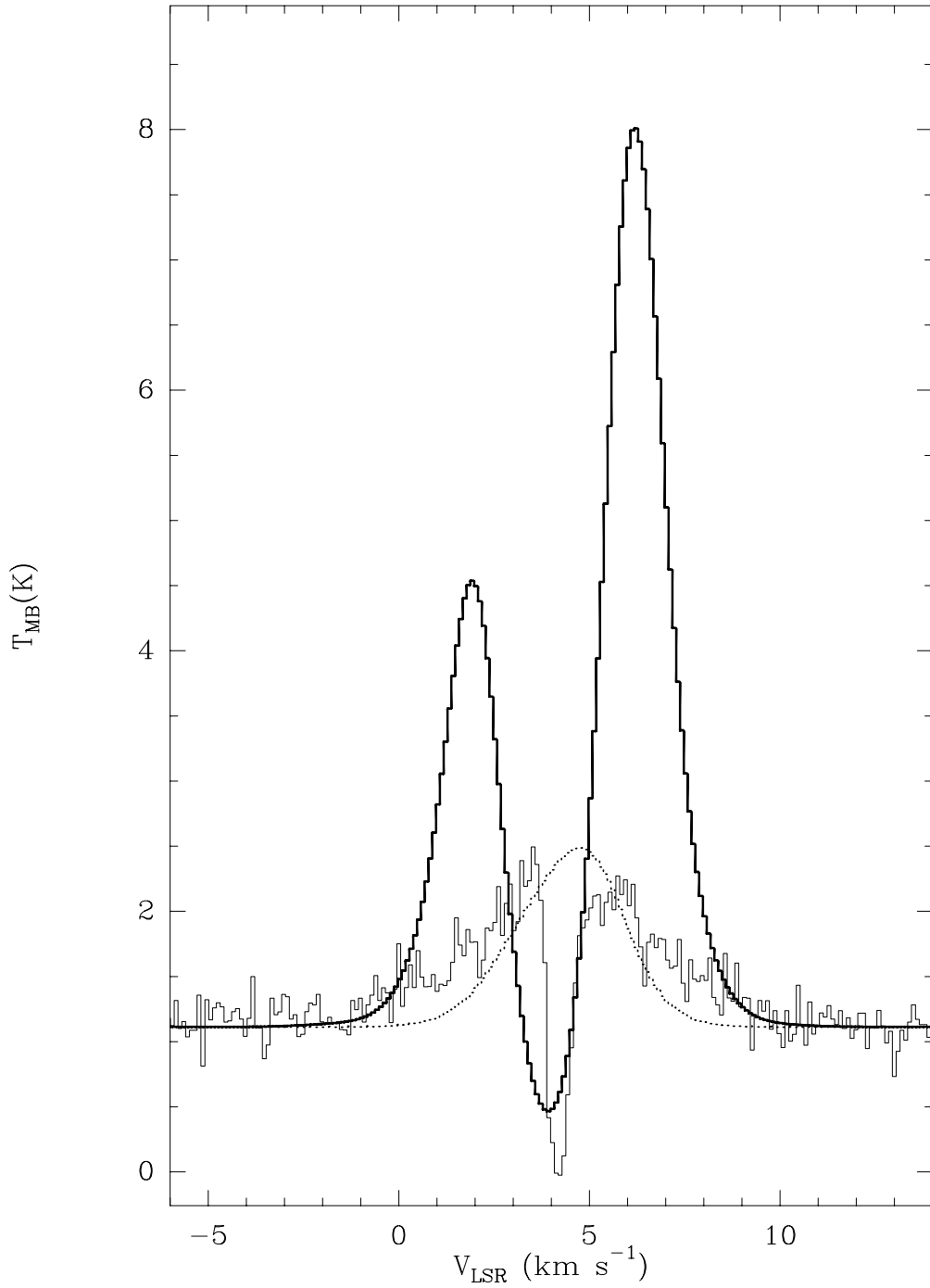


Fig. 15.— Spectrum of the observed HDO ground-state transition overlaid with outflow model spectra for  $[\text{HDO}]/[\text{H}_2]$  abundances of  $3 \times 10^{-10}$  (dotted) which matches the level of the maximum emission, and  $3 \times 10^{-9}$  (thick) which fits the outer wings.

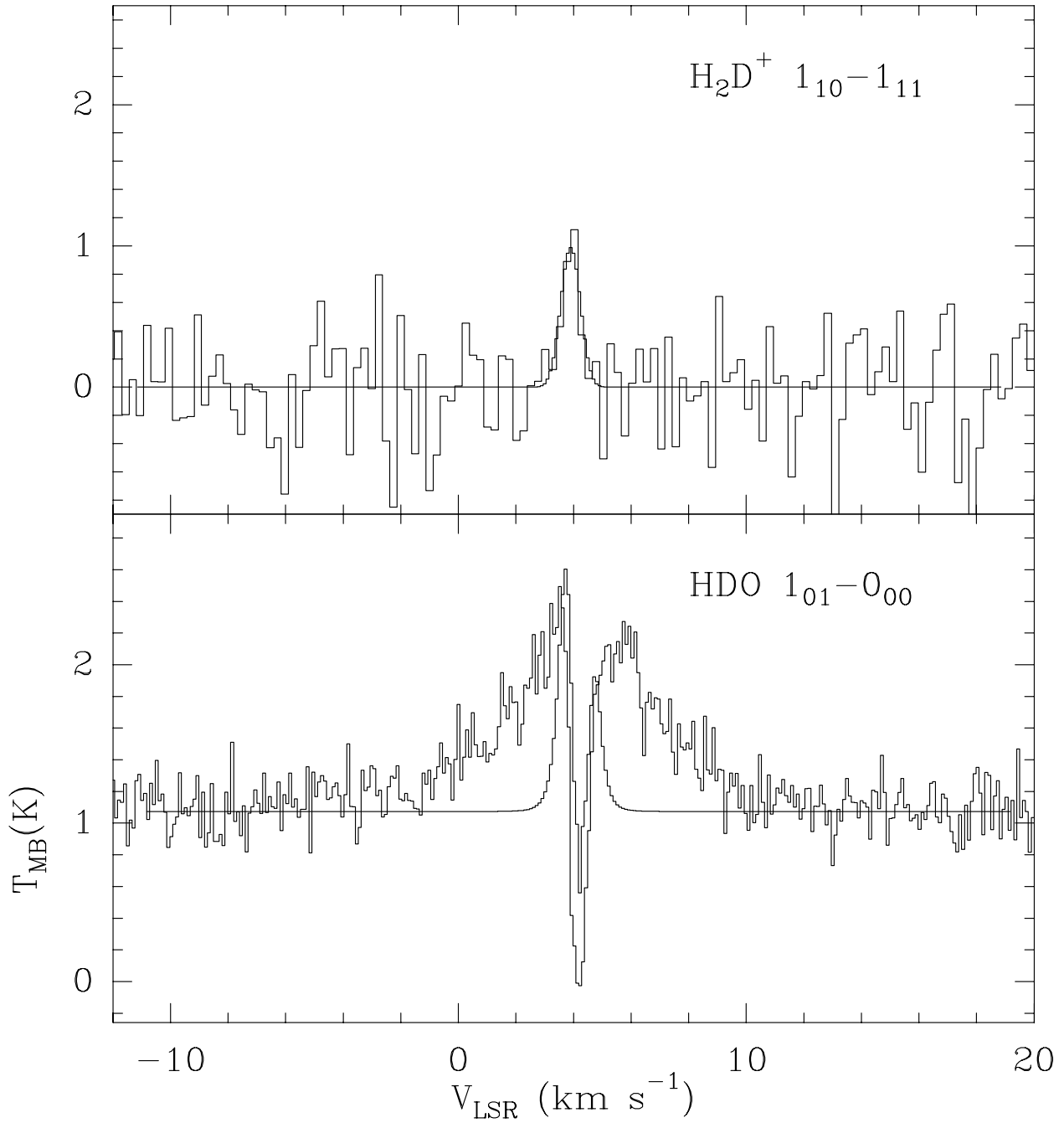


Fig. 16.— Model spectra obtained from the chemical calculations for an infalling envelope, overlaid on the observed  $\text{H}_2\text{D}^+ 1_{10}-1_{11}$  (top) and  $\text{HDO } 1_{01}-0_{00}$  (bottom) observations.

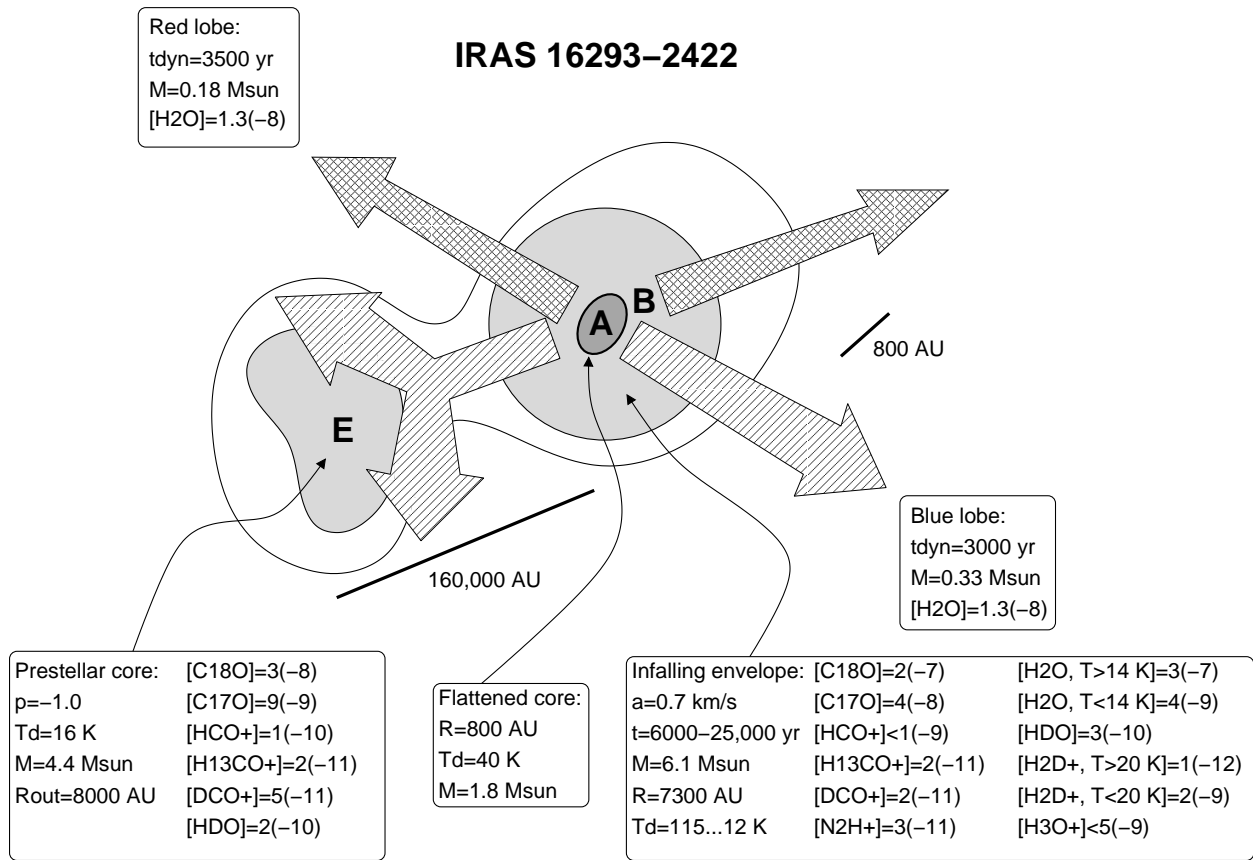


Fig. 17.— Schematic overview of the IRAS 16293-2422 region showing its distinct physical regions with their derived physical parameters, and molecular abundances.